

00-62

182401

**STRUCTURAL DAMAGE SIMULATIONS ACCOUNTING  
FOR INERTIAL EFFECTS AND IMPACT  
AND OPTIMIZATION OF GRID-STIFFENED  
NON-CIRCULAR SHELLS**

**- FINAL REPORT -**

**for**

**NASA Grant NCC-1-284**

Submitted to:

Structural Mechanics Branch  
Structures Division  
NASA Langley Research Center  
Hampton, Virginia 23681-0001  
Dr. Damodar Ambur, Technical Monitor

by the

Department of Aerospace Engineering  
College of Engineering and Technology  
Old Dominion University

Principal Investigator:

Chuh Mei, Ph. D.

Professor of Aerospace Engineering

Research Associate:

Navin Jaunky, Ph. D.

Old Dominion University

Norfolk, Virginia 23529-0247

Telephone No. (757) 683-3733

FAX No. (757) 683-3200

Email: [chmei@aero.odu.edu](mailto:chmei@aero.odu.edu)

November 8, 1999

# STRUCTURAL DAMAGE SIMULATIONS ACCOUNTING FOR INERTIAL EFFECTS AND IMPACT AND OPTIMIZATION OF GRID-STIFFENED NON-CIRCULAR SHELLS

Final Report  
NASA Grant NCC-1-284

by

Chuh Mei.

Department of Aerospace Engineering  
College of Engineering and Technology  
Old Dominion University

## SUMMARY

The goal of this research project is to develop modelling and analysis strategy for the penetration of aluminium plates impacted by titanium impactors. Finite element analysis is used to study the penetration of aluminium plates impacted by titanium impactors in order to study the effect of such uncontained engine debris impacts on aircraft-like skin panels. LS-DYNA3D ) is used in the simulations to model the impactor, test fixture frame and target barrier plate. The effects of mesh refinement, contact modeling, and impactor initial velocity and orientation were studied. The research project also includes development of a design tool for optimum design of grid-stiffened non-circular shells or panels subjected to buckling.

This research activity extended over a period of four years from January 1, 1999 until October 31, 1999. Over the course of the grant, a post doctoral research assistant was supported.

## BACKGROUND

Prediction of the elasto-plastic, large-deformation, transient dynamic behavior involving impact of multiple deformable bodies continue to provide new insight into the response of complex structural systems subject to extreme loading conditions or exposed to extreme environments. Much of the computational mechanics technology has evolved over a decades of research sponsored by government laboratories which also have had access to large supercomputer facilities. The rapid development of affordable computer technology with high-speed processors, large memories, and large, fast secondary storage devices has contributed to the integration of these analysis tools within the design and analysis groups in industry. This technology transfer has provided methods and software that can be used to improve designs, reduce uncertainties, and increase product safety.

One such application involves simulating the response of a fuselage skin when impacted by debris. Developing accurate finite element models and analysis strategies for this event has the potential of significantly improving the design, reliability, and safety of engines, especially for commercial transport applications. Two potential hazards are the subject of ongoing research efforts. The one event involves containing failed engine debris within the engine housing - contained failure. The other event involves the potential impact of uncontained failed engine debris on other parts of the aircraft - uncontained failure.

The potential hazard resulting from an uncontained turbine engine failure has been a long-term concern of the Federal Aviation Administration (FAA), National Aeronautical and Space Administration (NASA), and the aircraft industry. For the purpose of airplane evaluations, the FAA defines an uncontained failure of a turbine engine as any failure which results in the escape of rotor fragments from the engine or Auxiliary Power Unit (APU) that could result in a hazard. A contained failure is one where no fragments are released through the engine structure; however, fragments may be ejected out the engine air inlet or exhaust. Rotor failures which are of concern are those where released fragments have sufficient energy to create a hazard to the airplane and its passengers.

Failed rotating components can release high-energy fragments which are capable of penetrating the engine cowling and damaging the fuel tank, hydraulic lines, auxiliary power units, and other accessories. The penetration capability of the material released is affected by its shape, orientation of impact, material properties, and kinetic energy. The high-energy fragments are dispersed circumferentially in all directions at very high velocities. When the fragments escape or penetrate the engine casing, the consequences can range from minor to catastrophic. These fragments, released during failure, affect the flying performance of the aircraft in a number of direct or indirect ways, and impact and damage surrounding structures and equipment. Behaving as projectiles, these fragments have damaged surrounding runways, residences and vehicles.

Simulations of the penetration of aluminium plates impacted by titanium fragments using the LS-DYNA3D nonlinear transient dynamics finite element code were carried out. These simulations are related to the impact and penetration scenario that would result in the event of uncontained engine debris striking the fuselage skin. This investigation assesses the spatial discretization needs in the vicinity of the impact, material models for tearing and failure, finite element type selection, and the contact modeling for penetration and damage. Selected parametric studies related to impactor initial speed and orientation were performed.

Under this objective, a design tool for the optimum design of grid-stiffened composite non-circular shells with global and local buckling constraints, and strength constraints using a discrete optimizer has been developed. Aircraft and other flight vehicle structures are often built up of non-circular panels or shells.

## RESEARCH OBJECTIVES AND ACCOMPLISHMENTS

The goal of this research project was to develop and assess methodologies for the design and analysis of fuselage structures. Specific research objectives were as followed:

### High Energy Testing of Structures.

A gas-actuated penetration device has been used for high-energy impact testing of structures. The high-energy impact testing is for experimental simulation of uncontained engine failures. The non-linear transient finite element code LS-DYNA3D has been used in the numerical simulations of a titanium rectangular blade with an aluminum target plate. Threshold velocities for different combinations of pitch and yaw angles of the impactor were obtained for the impactor-target test configuration in the numerical simulations. Complete penetration of the target plate was also simulated numerically. Finally, limited comparison of analytical and experimental results is presented for complete penetration of the target by the impactor. The complete research activity is reported in Appendix A.

## Optimal Design of Grid-stiffened Panel and Shells with Variable Curvature.

A design strategy for optimal design of composite grid-stiffened panels with variable curvature subjected to global and local buckling constraints is developed using a discrete optimizer. An improved smeared stiffener theory is used for the global buckling analysis. Local buckling of skin segments is assessed using a Rayleigh-Ritz method that accounts for material anisotropy and transverse shear flexibility. The local buckling of stiffener segments is also assessed. Design variables are the axial and transverse stiffener spacing, stiffener height and thickness, skin laminate, and stiffening configuration, where stiffening configuration is herein defined as a design variable that indicates the combination of axial, transverse and diagonal stiffeners in the stiffened panel. The design optimization process is adapted to identify the lightest-weight stiffening configuration and stiffener spacing for grid-stiffened composite panels given the overall panel dimensions, in-plane design loads, material properties, and boundary conditions of the grid-stiffened panel. The complete research activity is reported in Appendix B. The results of the research will be presented at the AIAA/ASME/ASCE/AHS/ASC 41<sup>th</sup> Structures, Structural Dynamics, and Materials Conference, April 2-6, 2000, Atlanta, GA.

## APPENDIX A

### High Energy Testing of Structures.

## Abstract

A gas-actuated penetration device has been used for high-energy impact testing of structures. The high-energy impact testing is for experimental simulation of uncontained engine failures. The non-linear transient finite element code LS-DYNA3D has been used in the numerical simulations of a titanium rectangular blade with an aluminum target plate. Threshold velocities for different combinations of pitch and yaw angles of the impactor were obtained for the impactor-target test configuration in the numerical simulations. Complete penetration of the target plate was also simulated numerically. Finally, limited comparison of analytical and experimental results is presented for complete penetration of the target by the impactor.

## Introduction

The potential hazard resulting from an uncontained turbine engine failure has been a long-term concern of the Federal Aviation Administration (FAA), National Aeronautical and Space Administration (NASA), and the aircraft industry (e.g., Refs. [1]-[5]). For the purpose of airplane evaluations, the FAA defines an uncontained failure of a turbine engine as any failure which results in the escape of rotor fragments from the engine or Auxiliary Power Unit (APU) that could result in a hazard (Refs. [4] and [5]). A contained failure is one where no fragments are released through the engine nacelle structure; however fragments may be ejected from the engine air inlet or exhaust. Rotor failures that are of concern are those where released fragments have sufficient energy to create a hazard to the airplane and its passengers.

Accepting that the failures will continue to occur in service, attempts are made to contain all debris within a strengthened structure (e.g., see Refs. [6]-[9]). Design and test requirements are imposed on the engine nacelle to ensure some containment capability. Engine nacelle design and test requirements are covered in the United States Code of Federal Regulations, Title 14, Aeronautics and Space, Part 33, Airworthiness Standards; Aircraft Engines ([1]). Part 33 of the Federal Aviation Regulations (FAR) has always required the engine nacelle to be designed to contain damage resulting from rotor blade failure. The containment of failed rotor blades is a complex process which involves high energy, high speed interactions of numerous locally and remotely located engine components (such as failed blade, other blades, containment structure, adjacent cases, bearings, bearing supports, shafts, vanes and externally mounted components). Once failure begins, secondary events of a random nature may occur whose course cannot be precisely predicted (e.g., [4]).

Therefore, assuming that uncontained debris will continue to be generated, design considerations outlined in the AC 20-128A (e.g., [5]) provide guidelines for achieving the desired objective of minimizing the hazard to an airplane from uncontained rotor failure. These guidelines assume a rotor failure will occur and that analysis of the effects of this failure is necessary. The designs intend to make the aircraft invulnerable to the debris by such means as deflection, the judicious location of critical parts, hydraulic lines, and structure, suitable redundancy where appropriate. Given that the damage is uncontained, developing an understanding of the impact event of the engine fragments or other parts of the structure is needed. FAA Advisory Circular AC 20-128A (e.g., [5]) provides specifications for fragment sizes to be used in the safety analysis models. The fragment size includes a single disc with

blades fragment, that is, with one-third of blade height and one-third of the mass of the disc with blades, intermediate fragments with one-third of the disc with blades radius with a mass of 1/30th of the disc with blades, and small fragments (shrapnel) ranging in size up to a maximum dimension corresponding to the tip half of the blade airfoil.

Assuming that the large engine fragments released in the radial direction of the engine are contained by the engine containment structure, experimental studies and analytical simulations are still necessary to understand the effect of small engine fragments ejected from the engine air inlet or exhaust on the surrounding structures. Designing aircraft structures to either withstand this threat or to perform safely after the threat occurs requires an understanding of the response of structures subjected to high-energy impacts from these small engine fragments. Although some high-energy penetration work has been conducted related to the development of engine containment structures (e.g., Refs. [1]-[8]), there is very little reported research (e.g., Refs. [10]-[12]) on metallic and composite airframes when this type of high-energy threat occurs. The main objectives of the present paper are to discuss the development of a high-energy impact device capable of projecting small impactor plates that are representative of small engine fragments (0.6-lb weight), and to present results from numerical simulations. The analysis efforts presented in this study address:

- a. The threshold velocity for the impactor to penetrate the test specimen when impacted at normal incidence to the target.
- b. The threshold velocities for no penetration when the impactor strikes the target at attitudes that are combinations of pitch, roll and yaw directions.
- c. To compare the analysis results with preliminary target penetration test results.

### Gas-actuated Penetration Device

A photograph of the gas-actuated penetration device is shown in Figure 1 (a). The pressure chamber is connected to the barrel of the device through a diaphragm chamber. When the pressure differential across the diaphragm reaches a predetermined value, the diaphragm ruptures and the gas propels a sabot located in the barrel. The sabot is a hollow cylindrical body made of a plastic material with a provision in it to hold an impactor plate. The sabot is guided as it travels along the barrel so that the impactor plate orientation is not altered significantly before it impacts the target test specimen. When the sabot reaches the end of the barrel, a splitter arrangement in the muffler assembly engages the sabot and releases the impactor plate which travels farther and impacts the target. A photograph of the test specimen mounted in a picture frame fixture in front of the barrel is shown in Fig. 1(b). The box surrounding the test specimen is used as an impactor containment structure and is filled with sand bags.

The specimen penetration device is designed such that the impactor plate located in the sabot is projected at the target with specified tolerances on its attitude. Since the device will be used for composite structures which have directional properties, these tolerances are necessary to ensure that the impactor contacts the target at a given orientation with respect to its material axis. The goals for the tolerances in pitch, roll, and yaw angles are 2 degrees which is consistent with the tolerance used in manufacturing laminated composite structures.

## Numerical Simulation Tools

Finite element simulations of structural problems involve pre-processing, analysis and postprocessing. For the impact and penetration simulations, the pre-processing step is performed using the INGRID computer code (Ref. [13]). The analysis step involves the nonlinear transient dynamic response prediction for the dynamic behavior prior to impact, the nonlinear impact and penetration event itself, and the subsequent dynamic behavior. The LS-DYNA3D computer code (Refs. [14, 15]) has been used for the analyses here. Additional details are provided in Ref. [16].

Penetration of the target plate can be simulated in two ways depending on the modeling approach used for the target plate. Using the approach of tied nodes with failure, coincident nodes are generated in selected regions and then tied together with a constraint relation. In the LS-DYNA3D code, these tied nodes remain together until the volume-weighted effective plastic strain, averaged over all elements connected to the nodes in a given constraint, exceeds a specified value. This approach is referred to herein as the TNWF approach. Once this value is exceeded, all nodes in that constraint are released to simulate the initiation of a crack, fracture or penetration. In the second approach, called the element erosion approach (or EE approach), the finite element model is generated in the standard manner without requiring duplicate coincident nodes. Once the effective plastic strain in an element reaches a specified critical value, the element is removed from the computations. In this approach, elements do not separate from the initial finite element model and, hence, tracking the rigid-body motion of these newly created fragments is not necessary. The LS-TAURUS computer code (e.g., Refs. [14, 15]) is used for postprocessing.

### Configuration studied and Modeling

The target configuration considered in the present study is shown in Figure 2. This configuration is representative of the test setup shown in Figure 1 (b). An aluminum target plate is clamped between two steel frames and a titanium impactor may have pitch and yaw angles as shown in the figure. The material properties for aluminum, steel and titanium are given in Table 1. An elastic-plastic strain-hardening material model is used within LS-DYNA3D (Material Type 3 of Refs. [14, 15]) in the TNWF approach. Material type 24 of Refs. [14, 15] is used within LS-DYNA3D for the EE approach. Material 24 is elastic-plastic with a bilinear stress-strain curve.

The frame that supports the aluminum target plate and impactor are modeled using 8-node solid elements while the target is modeled using 4-node Belytschko-Lin-Tsay shell elements. The impactor has a node distribution of 9 by 4 by 16 in the x, y, and z directions respectively, or 576 nodes with 360 elements. Using the INGRID (Ref. [13]) preprocessor, the impactor is initially positioned at the center and 0.25 in. away from the target. The impactor may then be pitched or yawed by two degrees as required. When the impactor is pitched by two degrees, it has to be translated by -0.1362 in. in the y-direction. Similarly, when the impactor is yawed by two degrees it has to be translated by -0.1362 in. in the z-direction. These translations are necessary since the impactor is moving along the its orientation as shown in Figure 2. The translations are computed based on the distance between the impactor and the target in the gas launcher-target arrangement. The velocity of the impactor is  $V_0 \cos(\alpha_p) \cos(\alpha_y)$  in the x-direction,  $-V_0 \sin(\alpha_p)$  in the y-direction and

$-V_0 \cos(\alpha_p) \sin(\alpha_y)$  in the z-direction, where  $\alpha_p$  and  $\alpha_y$  are the pitch and yaw angles, respectively, and  $V_0$  is the speed of the impactor. All of the nodes of the impactor are prescribed with these velocity components.

The area with the dashed-line boundary as shown in Figure 2 is herein referred to as the shell-break area and consists of coincident nodes which are tied together with a constraint relation. This approach for penetration modeling of tied-nodes-with-failure (TNWF) is used to simulate penetration of the target by the impactor. In the LS-DYNA3D code (Refs.[14, 15]), these tied nodes remain together until the volume-weighted effective plastic strain, averaged over all elements connected to the coincident nodes in a given constraint, exceeds a specified value. The specified plastic strain value for aluminum is 0.2 which is the ultimate strain at failure. Two meshes are considered in the case of TNWF approach;

- Mesh TNWF-1 has a shell break area of  $8 \times 2$  inches. The shell break area is centered about the axes shown in Figure 2. The model contains 11,730 nodes, 1,896 8-node solid elements, and 4,408 4-node shell elements. The element size in the shell break area (or TNWF area) is  $0.05 \times 0.20$  inch in the y and z direction respectively. The finite element discretization of the target plate is shown in Figure 3.
- Mesh TNWF-2 has a shell break area of  $8 \times 6$  inches. The shell break area is centered in the y-direction, and the top edge of the shell break area is 1.0 inch above  $z = 0$  with respect to the axes shown in Figure 2. The model contains 16,770 nodes, 2,896 8-node solid elements, and 6,232 4-node shell elements. The element size in the shell break area is still  $0.05 \times 0.20$  inch in the y and z direction respectively. The finite element discretization of the target plate is shown in Figure 4.

In the element erosion (EE) approach, the specified critical value for the plastic strain is 0.2 which is the ultimate strain for failure. The time step for element deletion is  $7.0E-08$  second which is less than the minimum time step size in the simulation. A time step size for element deletion is required for Material Type 24. Two types of meshes were considered.

- Mesh EE-1 has a refined area of the same size and location as the Mesh TNWF-1, except that the element size in the refined area is  $0.05 \times 0.05$  inch in the y and z direction respectively. Hence Mesh EE-1 is more refined than Mesh TNWF-1. The model contains 18,519 nodes, 3,471 8-node solid elements, and 13,528 4-node shell elements. The finite element discretization of the target plate is shown in Figure 5.
- Mesh EE-2 has a refined area of the same size and location as the Mesh TNWF-2, except that the element size in the refined area is  $0.05 \times 0.05$  inch in the y and z direction respectively. Hence Mesh EE-2 is more refined than Mesh EE-1 and Mesh TNWF-2. The model contains 34,311 nodes, 8,832 8-node solid elements, and 27,768 4-node shell elements. The finite element discretization of the target plate is shown in Figure 6.

Reference [17] addresses the modelling issues on the impact of aluminum target with titanium projectile.

Contact or impact algorithms have always been an important capability in the DYNA3D family of codes. Contact may occur along surfaces of a single body undergoing large deformation, between two or more deformable bodies, or between a deformable body and a rigid barrier. In the present study, the sliding interface with friction and separation approach (LS-DYNA3D, Interface Type 3) is used to model the impact event between the impactor and target plate, and the friction coefficients are prescribed to be equal to zero. The bounding surface of the three-dimensional impactor is treated as the slave surface, and the target plate as the master surface.

The LS-DYNA3D code permits automatic examination of the finite element mesh and material properties in order to determine an appropriate time step size for numerical stability. This time step size is then automatically adjusted throughout the transient analysis to account for contact and local material and geometric nonlinearities.

### Results and Discussion

Analytical simulation results obtained using the LS-DYNA3D code are reported in this section for the target configuration described in Figure 2. The modeling features discussed in the previous section were used. The finite element studies are based on the assessment of the time variation of the axial velocity of the centroid of the impactor, the time variation of the contact force in the axial direction, and the maximum plastic strain on the target.

Results are presented for the following cases with different initial impactor velocity ( $V_0$ ) and different pitch ( $\alpha_p$ ), roll ( $\alpha_r$ ) and yaw ( $\alpha_y$ ) angles of the impactor;

- Case 1:  $V_0 = 3,000$  in/sec (250 ft/sec),  $\alpha_p = 0$  degrees,  $\alpha_r = 0$  degrees,  $\alpha_y = 0$  degrees.
- Case 2:  $V_0 = 3,000$  in/sec (250 ft/sec),  $\alpha_p = 0$  degrees,  $\alpha_r = 0$  degrees,  $\alpha_y = 2$  degrees.
- Case 3:  $V_0 = 2,640$  in/sec (220 ft/sec),  $\alpha_p = 2$  degrees,  $\alpha_r = 0$  degrees,  $\alpha_y = 0$  degrees.
- Case 4:  $V_0 = 2,760$  in/sec (230 ft/sec),  $\alpha_p = 2$  degrees,  $\alpha_r = 0$  degrees,  $\alpha_y = 2$  degrees.
- Case 5:  $V_0 = 5,400$  in/sec (450 ft/sec),  $\alpha_p = 0$  degrees,  $\alpha_r = 0$  degrees,  $\alpha_y = 0$  degrees.
- Case 6:  $V_0 = 5,400$  in/sec (450 ft/sec),  $\alpha_p = 4.7$  degrees,  $\alpha_r = 4.76$  degrees,  $\alpha_y = 0$  degrees.
- Case 7:  $V_0 = 5,400$  in/sec (450 ft/sec),  $\alpha_p = 0$  degrees,  $\alpha_r = 4.76$  degrees,  $\alpha_y = 0$  degrees.
- Case 8:  $V_0 = 12,000$  in/sec (1000 ft/sec),  $\alpha_p = 4.7$  degrees,  $\alpha_r = 4.76$  degrees,  $\alpha_y = 0$  degrees.

Case 1 through 4 are intended to simulate the rebound test with the aluminum target plate. Case 5 through 8 are intended to simulate penetration test with the aluminum target. The damage result from these analyses case are used to compare with the corresponding experimental results for complete penetration of the target.

Analytical simulations for Case 1 through 4 were performed to determine the threshold velocity for penetration for the different pitch and yaw angle combinations using TNWF

approach and Mesh TNWF-1. The threshold velocity is defined as the velocity above which the impactor will penetrate the target completely. The threshold velocity is an important quantity in selecting the initial impactor velocity for the gas launcher. The threshold velocity was determined by analyses to be the velocity for which the impactor rebounds from the target while creating partial perforation of the target or producing a maximum plastic strain that is marginally lower than the ultimate strain value of 0.2 for aluminum without penetration of the target.

### Simulation Parameters

To insure that a simulation analyses using the LS-DYNA3D code is meaningful, the analyst needs to monitor the time step size, the ratio of the sliding interface energy to the initial or total energy, and the nodal velocities. Since an explicit time integration algorithm is used in this code which automatically adapts the time step size as the plasticity and damage develop in the elements, the time step size may be driven to nearly zero. A problem with the simulation occurs for such a case. Similarly, if the maximum ratio of the sliding interface energy to the total energy ( $\text{Max}(\text{SIE} / \text{TE})$ ) is larger than 10%, then the sliding interface penalty factor (SIPF) has to be adjusted. A good goal is to keep this ratio to be under 10%. A high ratio of the sliding interface energy to the total energy may lead to a simulation problem where nodal velocities take on out-of-range values (e.g., Not a Number values). To achieve these goals in simulation, multiple analyses with the current finite element model and possible finite element remodeling is necessary to validate the simulation results.

The sliding interface penalty factor (SIPF) and the computed time step factor (CTSF) are two parameters among others that affect the simulation results. The variation in simulation results for Case 4 for different SIPF values is shown in Table 2 using TNWF approach and Mesh TNWF-1. The value for CTSF is 0.6 for all analyses. This value for CTSF does not lead to spikes in the time variation of the impactor axial velocity. Hence  $\text{CTSF} = 0.6$  is an appropriate value for the impactor velocities considered in Table 2. This value is also appropriate for the impactor velocities considered in the other simulations.

It can be seen from Table 2, that there are no simulation problems with Analysis Number 1 and 2, but the  $\text{Max}(\text{SIE} / \text{TE})$  values are 33% and 12% respectively. For Analysis Number 3 and 4, although the  $\text{Max}(\text{SIE} / \text{TE})$  values are well below 10%, there are simulation problems. Analysis Number 5 and 6 were carried out for a velocity of 230 ft/sec and although the  $\text{Max}(\text{SIE} / \text{TE})$  value is 4% for Analysis Number 5, there is a simulation problem. The  $\text{Max}(\text{SIE} / \text{TE})$  value is 8.5% for Analysis Number 6 which is considered to be acceptable and there is no simulation problem. In Analysis Number 6, the impactor rebounds from the target while creating a maximum plastic strain of 0.1972. Hence Analysis Number 6 is considered to provide meaningful results for the case when  $\alpha_p = \alpha_y = 2$  degrees. Since the maximum plastic strain is 0.1972 for Analysis Number 6,  $V_0 = 230$  ft/sec is considered close to the threshold velocity which can be obtained using Mesh TNWF-1.

Simulation for other cases were investigated in a similar manner to Case 4. The simulation parameters and results for Cases 1 through 4 are summarized in Table 3 using TNWF approach and Mesh TNWF-1. Reference [17] shows the effect of SIPF on the time variation of the total energy. Accordingly, there is a discontinuity in the total energy associated with the out-of-range velocities. The importance of simulation parameters for velocities that are close to the threshold velocity is also discussed in Ref. [17]. It can be seen from Table 3

that the  $\text{Max}(\text{SIE} / \text{TE})$  value is less than 10% for the cases considered. No simulation problems occurred up to the analysis termination time. At the analysis termination time, the impactor is away from the target and there is no contact with the target at all.

### Simulation Results for Rebound Cases

The impactor rebounds from the target for Cases 1 through 4 with residual velocities of -43.6, -99.5, -77.0, and -89.8 ft/sec, respectively as shown in Table 3. For Case 1, there is partial penetration of the target, whereas for Cases 2, 3 and 4, there is no partial penetration. However, in Cases 3 and 4, the maximum effective plastic strains are 0.1950 and 0.1972, respectively, which is close to the ultimate strain value of 0.2. Therefore, the initial velocities for Case 4 and 5 are considered close to the threshold velocity for the pitch and yaw angles considered. The initial velocity for Case 2 is not close to the threshold velocity for the yaw angle considered, since the maximum effective plastic strain is well below the ultimate strain of 0.2.

The axial velocity histories for the centroid of the impactor for Cases 1 through 4 are shown in Figure 7 and the axial contact force history for the target for Cases 1 through 4 are shown in Figure 8. The residual velocities for these cases are negative indicating rebound from the target. The differences between the axial velocity and axial contact force histories for Cases 1 through 4 are small due to the small differences in impactor velocity and pitch and yaw angles. Fringe plots for the effective plastic strain of the target for Case 1 and 4 at Time A and B as indicated in the axial contact force history in Figure 8 are shown in Figure 9 and 10 respectively. According to Figure 9 and 10, the effective plastic strain zone size for Case 1 is more or less same as that of Case 4, except for the partial perforation of the target that occurs in Case 1.

The threshold velocity for the impactor with zero pitch, roll and yaw angles obtained using element erosion approach (EE) using Mesh EE-1, is 200 ft/sec. This lower threshold velocity compared to Case 1 is due to Mesh EE-1 being a more refined mesh compared to Mesh TNWF-1. Hence Mesh TNWF-1 is a stiffer model compared to Mesh EE-1. The simulation was carried out with  $\text{SIPF} = 1.0\text{E-}03$ ,  $\text{CTSF} = 0.6$ , and the value of  $\text{Max}(\text{SIE} / \text{TE})$  obtained was 3.5 %. The axial velocity history obtained using EE approach and Mesh EE-1 is compared to that obtained using TNWF approach and Mesh TNWF-1 in Figure 11. It can be seen from Figure 11 that the residual velocity obtained using EE approach and Mesh EE-1 is same as that of Case 1. The axial contact force history of the target obtained using EE approach and Mesh EE-1 is compared to that obtained using from Case 1 in Figure 12. It can be seen that the axial contact force history is similar to that of Case 1, except for the peak contact force obtained using EE approach and Mesh EE-1 being about 16% lower than the peak contact force obtained from Case 1. This is again due to Mesh TNWF-1 being a stiffer model than Mesh EE-1. Therefore the threshold velocity of 200 ft/sec with zero pitch, roll, and yaw angle for the test configuration is very close to a converged value.

A comparison of the fringe plot of the effective plastic strain of the target for Case 1 and the effective plastic strain fringe plot obtained using EE approach and Mesh EE-1 is shown in Figure 13 at their respective termination time. The effective plastic strain zone for the coarse mesh (Mesh TNWF-1) is different from that of the fine mesh (Mesh EE-1). The partial perforation of the target plate by the impactor can be seen in Mesh TNWF-1 model.

In the Mesh EE-1 model, the impact event has produced two vertical cracks along the target plate. The damage obtained using Mesh EE-1 model is also symmetric.

### Simulation Results for Penetration Cases

A test was conducted with an impactor axial velocity of 450 ft/sec, and the impactor penetrated the aluminum target. On examining the damaged target, it was observed that the impactor made contact with the target at 1.19 inches below the center of the target and roll angle of the impactor was 4.76 degrees. The impactor had an initial roll angle of 5 degrees. This observation suggests that the impactor had a different pitch angle. The exact pitch angle is difficult to assess since some test conditions were unknown but an estimate of the pitch angle is 4.7 degrees. A photograph of the region around the impact site of the test target is shown in Figure 14. It can be seen that the impactor has punched a big hole in the target, resulting in petalling of part of the target and longitudinal cracks.

A parametric study that includes different pitch and roll angles, and different mesh discretization was carried out for the impactor speed of 450 ft/sec. The parametric study includes the following simulations;

- Study 1: Impactor attitude angles are  $\alpha_p = 0$  degree,  $\alpha_r = 0$  degree. TNWF approach is used with Mesh TNWF-1.
- Study 2: Impactor attitude angles are  $\alpha_p = 4.7$  degrees,  $\alpha_r = 4.76$  degrees. TNWF approach is used with Mesh TNWF-2.
- Study 3: Impactor attitude angles are  $\alpha_p = 0$  degree,  $\alpha_r = 4.76$  degrees. EE approach is used with Mesh EE-2.
- Study 4: Impactor attitude angles are  $\alpha_p = 4.7$  degrees,  $\alpha_r = 4.76$  degrees. EE approach is used with Mesh EE-2.

Fringe plots of the effective plastic strain of the target for these four simulations are at  $t = 1$  ms are shown in Figure 15. It can be seen that meshes Mesh TNWF-1 and Mesh TNWF-2 are not able to capture the cracks produced by the impact event which lead to a smaller hole being punched in the target. The longitudinal cracks are captured by Mesh EE-2 and the damage obtained in Study 3 and 4 are similar to that depicted in Figure 14. The axial velocity history and axial contact force history of the target are given in Figure 16. It can be seen that the axial velocity history for Study 3 and 4 are closed to each other and the axial contact force history of the target for Study 3 and 4 are also closed to each other. As observed before the peak contact force for the finer mesh is less than that of the coarser mesh, in this case by about 20%. A summary of simulation parameters and results for Study 1 through 4 is provided in Table 4.

Simulation results for Case 8 were obtained using EE approach and Mesh EE-2. The values used for SIFP and CTSF are  $1.0E-03$  and  $0.6$  respectively. The termination time was  $0.6$  ms. The  $\text{Max}(SIE / TE)$  is  $0.01\%$  and the residual axial velocity was  $975$  ft/sec. The fringe plot of the effective plastic strain of the target is shown in Figure 17, where it can be seen that the damage produced is similar to that of Study 1 through 4, except that the effective plastic strain is more localized around the hole. A comparison of the axial contact force history of the target with that of Study 4 is shown in Figure 18. It can be seen that the

peak contact force for Case 8 is close to that of Study 4. The duration of the axial contact force for Case 8 is much shorter than that of Study 4 owing to the higher initial velocity of the impactor for Case 8.

### Concluding Remarks

A gas-actuated penetration device has been developed for high-energy impact testing of structures. High-energy impact test was conducted for complete penetration of the target plate by a rectangular titanium plate impactor. Threshold velocities for different combinations of pitch and yaw angles of the impactor were obtained for the impactor-target test configuration in the numerical simulations using coarse and fine meshes. The analytical results suggests that the projectile attitude of  $\pm 2$  degrees donot significantly influence the target damage modes. Also projectile penetration through the aluminum target plate could potentially result in multiple cracks. Numerical simulation using very fine mesh predicted damage similar to that obtained from an experiment for complete penetration of the target by the impactor.

### References

- [1] Witmer, E. A. (Editor), *An Assessment of Technology for Turbojet Engine Rotor Failures*, Proceedings of a workshop sponsored by NASA Lewis Research Center and held at MIT on March 29-31, 1977, NASA CP-2017, August 1977.
- [2] Gerstle, J. H., "Analysis of Rotor Fragment Impact on Nallistic Fabric Engine Burst Containment Shields," *Journal of Aircraft*, Vol. 12, No. 4, April 1975, pp. 388-393.
- [3] Sarkar, S., and Atluri, S. N., "Impact Analysis of Rotor Fragments on Aircraft Engine Containment Structures," *Structural Integrity in Aging Aircraft*, C. I. Chang and C. T. Sun (editors), ASME, AD-Vol. 47, 1995, pp. 87-97.
- [4] Anon., "Turbine Engine Rotor Blade Containment/Durability," Federal Aviation Administration Advisory Circular No. 33-5, June 18, 1990.
- [5] Anon., "Design Considerations for Minimizing Hazards Caused by Uncontained Turbine Engine and Auxiliary Power Unit Rotor Failure," Federal Aviation Administration Advisory Circular No. 20-128A, March 25, 1997.
- [6] Le, D. D., *Evaluation of Lightweight Material Concepts for Aircraft Turbine Engine Rotor Failure Protection*, Federal Aviation Administration Report No. DOT/FAA/AR-96/110, July 1997.
- [7] Mathis, J. A., *Design Procedures and Analysis of Turbine Rotor Fragment Hazard Containment*, Federal Aviation Administration Report No. DOT/FAA/AR-96/121, March 1997.
- [8] Shockey, D. A., Giovanola, J. H., Simons, J. W., Erlich, D. C., Klopp, R. W., and Skaggs, S. R., *Advanced Armor Technology: Application Potential for Engine Fragment Barriers for Commercial Aircraft*, Federal Aviation Administration Report No. DOT/FAA/AR-97/53, September 1997.

- [9] Emmerling, William, Presentation Charts from the *Third FAA Workshop on Uncontained Engine Debris Characterization, Mitigation and Modeling*, held in San Diego, CA, October 28-30, 1997.
- [10] Zukas, J. A., Jones, G. H., Kimsey, K. D., Misesy, J. J., and Sherrick, T. M., "Three-Dimensional Impact Simulations: Resources and Results," *Computer Analysis of Large-Scale Structures*, K. C. Park and R. F. Jones, Jr. (editors), ASME, AMD-Vol. 49, 1981, pp. 35-68.
- [11] Whirley, Robert G., "Elasto-plastic Shell Analysis in DYNA3D," *Mechanical Engineering*, ASME, Vol. 113, No. 1, January 1991, pp. 56-60.
- [12] Dietz, D., "FEA Makes Airframes Safer," *Mechanical engineering*, ASME, Vol. 120, No. 1, January 1998, pp. 64-65.
- [13] Stillman, D. W., and Hallquist, J. O., "INGRID: A Three-Dimensional Mesh Generator for Modeling Nonlinear Systems," University of California, Lawrence Livermore National Laboratory, Report UCID-20506, 1985.
- [14] Anon., *LS-DYNA3D User's Manual*, Livermore Software Technology Corporation May 1, 1995.
- [15] Anon., *LS-DYNA3D Theoretical Manual*, Livermore Software Technology Corporation.
- [16] Lawson, Robin E., "LS-DYNA3D Modeling and Simulation for Uncontained Engine Debris Impact on Fuselage Skins," Master's Thesis, Department of Aerospace Engineering, Old Dominion University, Norfolk, VA, May 1999.
- [17] Knight, N. F., Jaunky, N., Lawson, R. E., and Ambur, D. A., "Modeling and Simulation for Uncontained Engine Debris Impact on Fuselage Skins using LS-DYNA3D," presented at AIAA/ASME/ASCE/AHS/ASC 40<sup>th</sup> Structures, Structural Dynamics, and Materials Conference, April 12-15, 1999, St. Louis, MO, AIAA-CP Paper No. 99-1573.

Table 1 Material properties for aluminum, titanium, and steel.

	Aluminum (2024-T3)	Titanium (Ti-6Al-4V)	Steel (A36)
Young's modulus (Msi)	10.0	16.0	30.0
Poisson's ratio	0.30	0.30	0.30
Yield strength (Msi)	0.05	0.12	0.35
Tangent modulus (Msi)	0.10	0.30	0.15
Hardening parameter	0.20	0.20	0.23
Weight density (lbs/in <sup>3</sup> )	0.10	0.16	0.28
Ultimate strain to failure (in/in)	0.20	-	-

Table 2 Effect of SIPF on numerical simulation results for Case 4 using TNWF approach and Mesh TNWF-1.

Analysis No.	Initial velocity, $V_0$ , ft/sec	SIPF <sup>a</sup>	CTSF <sup>b</sup>	Max(SIE / TE) <sup>c</sup>	Termination time, ms
1	250	0.25E-03	0.60	33%	1.8
	Remark: Maximum effective plastic strain is 0.152, impactor rebound.				
2	250	0.35E-03	0.60	12%	1.8
	Remark: Maximum effective plastic strain is 0.187, impactor rebound.				
3	250	0.55E-03	0.60	4.8%	1.8
	Remark: Target plate penetration and out-of-range velocities at 1.5 ms.				
4	250	0.45E-03	0.60	6.1%	1.8
	Remark: Target plate penetration and time step size driven to zero at t=1.317 ms.				
5	230	0.45E-03	0.60	4%	1.8
	Remark: Target plate perforation and impactor rebound. Out-of-range velocities at 1.14 ms				
6	230	0.35E-03	0.60	8.5%	1.9
	Remark: Maximum effective plastic strain is 0.1972 and impactor rebound.				

<sup>a</sup>SIPF = sliding interface penalty factor

<sup>b</sup>CTSF = computed time step factor

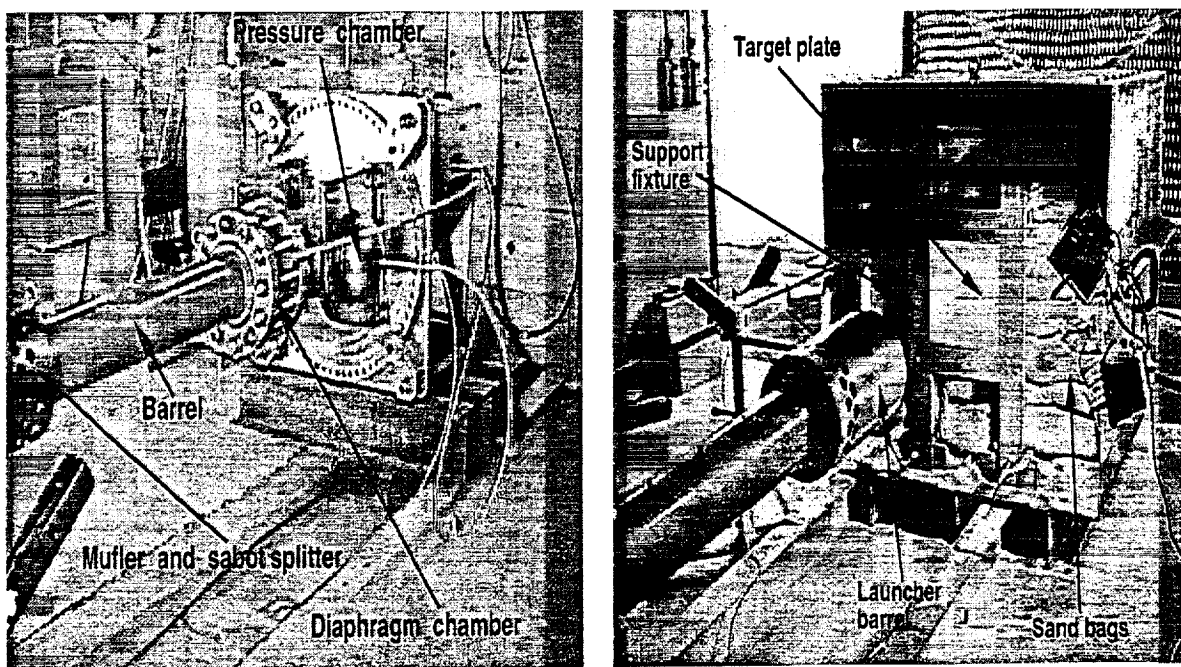
<sup>c</sup>Max(SIE / TE) = maximum sliding interface energy to total energy

Table 3 Summary of simulation parameters and results for Cases 1 through 4, (rebound cases) using TNWF approach and Mesh TWNF-1.

Case No.	1	2	3	4
Initial velocity, $V_0$ (ft/sec)	250	250	220	230
$(\alpha_p, \alpha_y)$ degree	(0,0)	(0,2)	(2,0)	(2,2)
Termination time (ms)	1.8	1.8	1.8	1.9
SIPF ( $\times 10E-03$ )	0.75	0.25	0.65	0.35
CTSF	0.6	0.6	0.6	0.6
Max(SIE / TE) %	2.2	2.2	6.0	8.5
Residual velocity (ft/sec) (axial direction)	-43.6	-99.5	-77.0	-89.8
Maximum plastic strain	0.2000	0.1460	0.1950	0.1972
Target penetration	partial	NO	NO	NO

Table 4 Summary of simulation parameters and results for Study 1 through 4, (penetration cases,  $V_0 = 450$  ft/sec).

Study No.	1	2	3	4
$(\alpha_p, \alpha_r)$ deg.	(0,0)	(4.7,4.76)	(0,4.76)	(4.7,4.76)
Termination time (ms)	1.0	1.0	1.0	1.0
SIPF ( $\times 10E-03$ )	0.5	0.2	1.0	1.0
CTSF	0.6	0.6	0.6	0.6
Max(SIE / TE) %	1.0	1.4	1.1	1.2
Residual velocity (ft/sec) (axial direction)	334.7	377.8	398.1	401.1



(a) Projectile launcher

(b) Target plate assembly

Figure 1: Photograph of the gas-actuated projectile launcher and test setup.

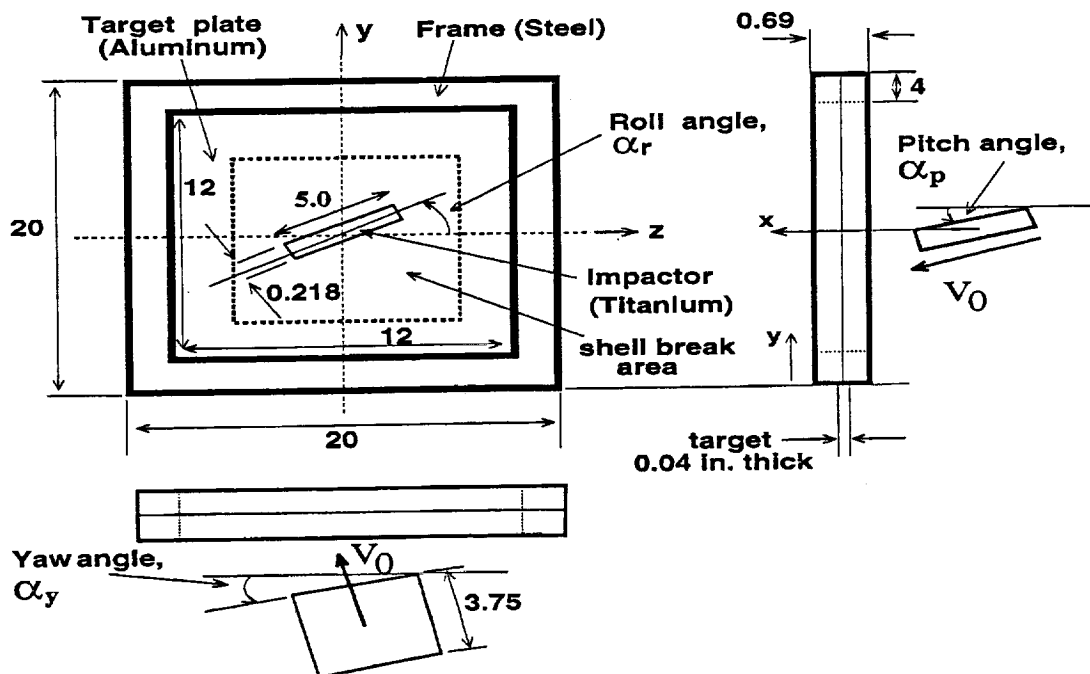


Figure 2: Dimensions for the test configuration. (Not to scale. All dimensions in inches.)

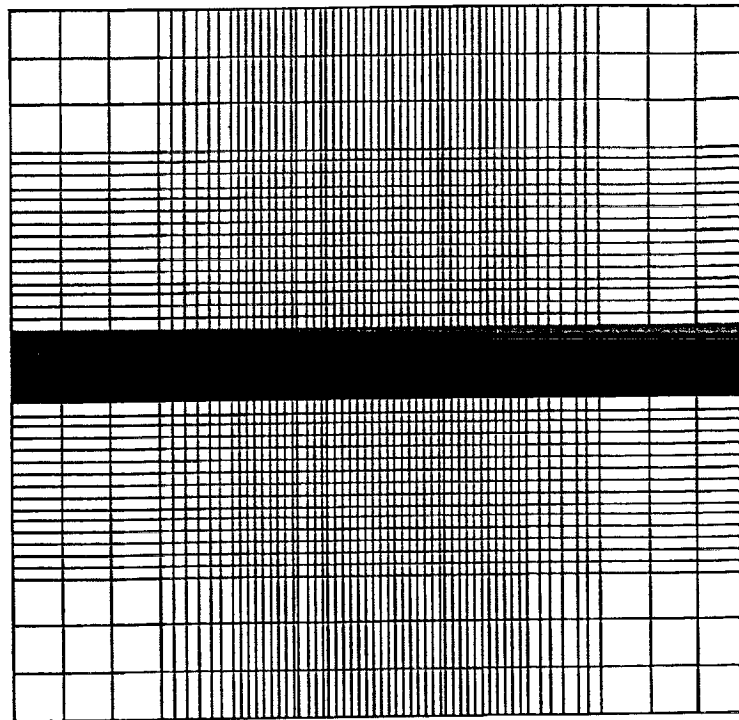


Figure 3: Finite element discretization of target plate for Mesh TNWF-1.

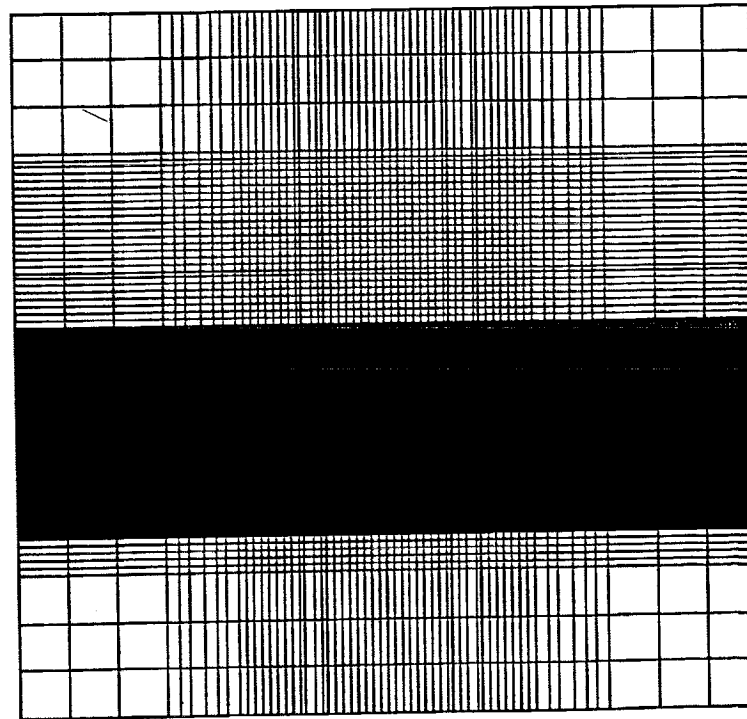


Figure 4: Finite element discretization of target plate for Mesh TNWF-2.

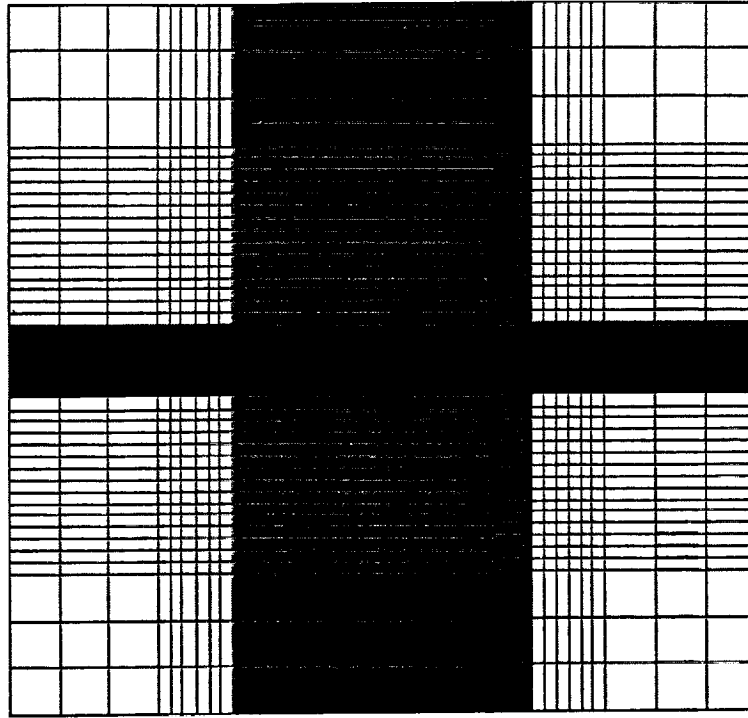


Figure 5: Finite element discretization of target plate for Mesh EE-1.

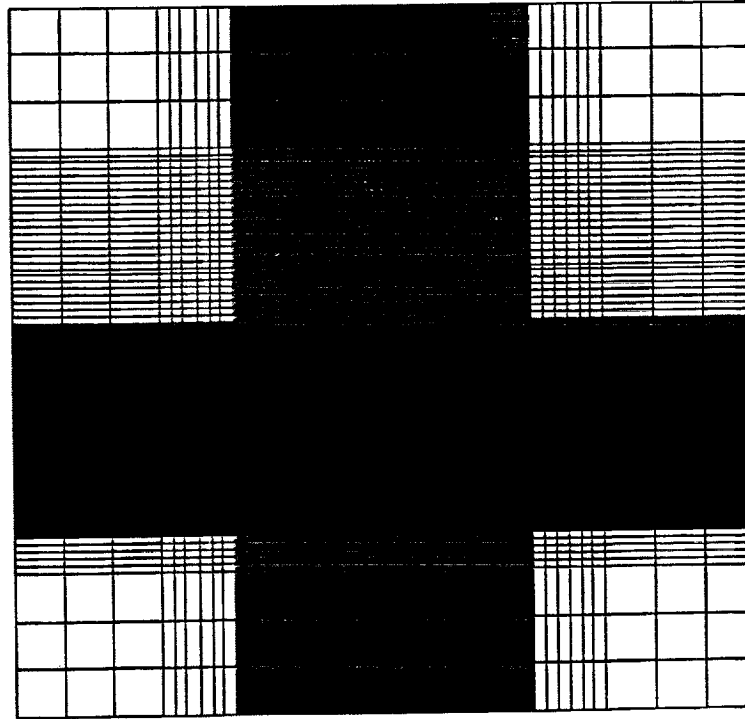


Figure 6: Finite element discretization of target plate for Mesh EE-2.

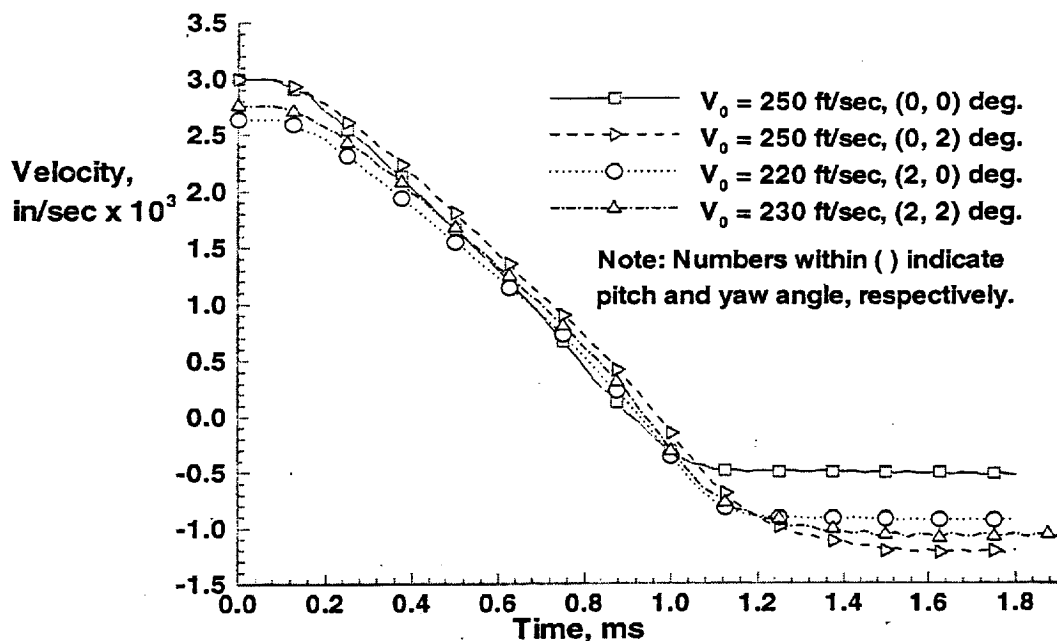


Figure 7: Axial velocity history of impactor for simulation Cases 1 through 4 using TNWF approach and Mesh TNWF-1.

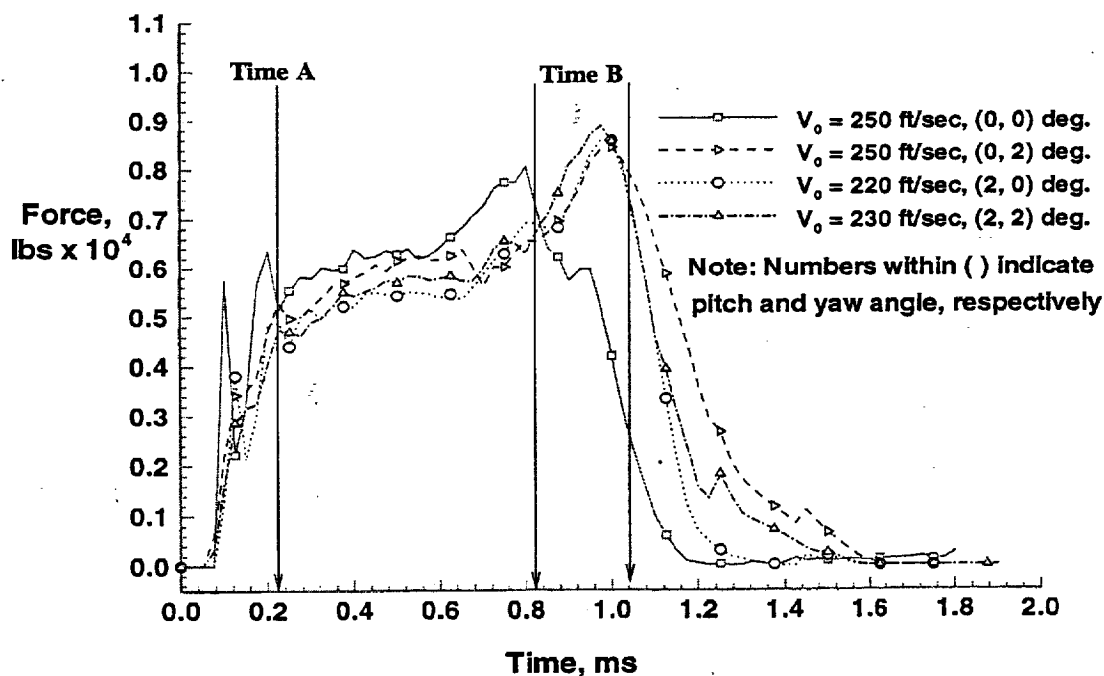


Figure 8: Axial contact force history of target for simulation Cases 1 through 4 using TNWF approach and Mesh TNWF-1.

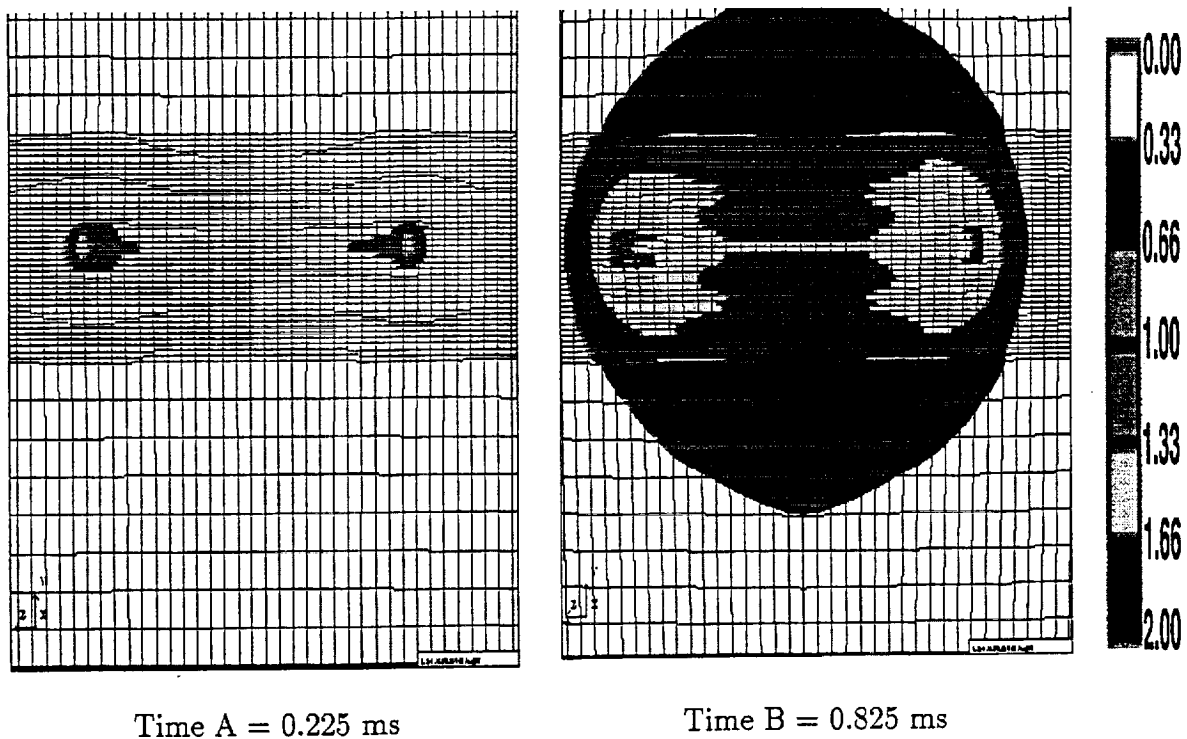


Figure 9: Effective plastic strain contours of the target for Case 1 using TNWF approach and Mesh TNWF-1 in the vicinity of impact site.

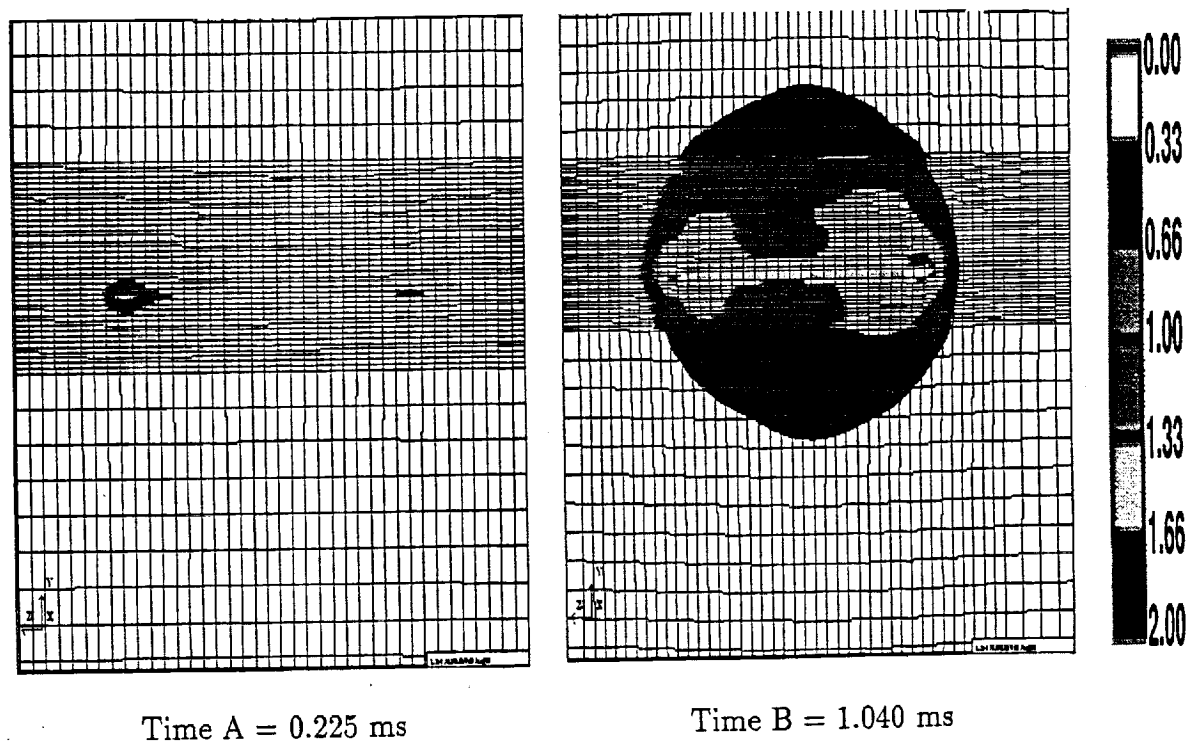


Figure 10: Effective plastic strain contours of the target for Case 4 using TNWF approach and Mesh TNWF-1 in the vicinity of the impact site.

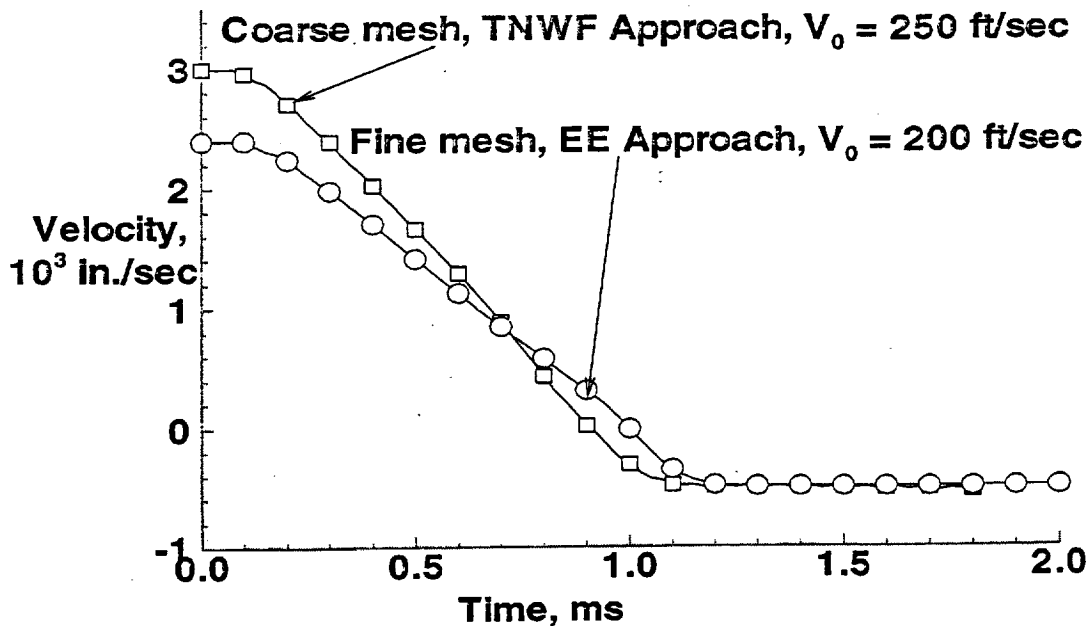


Figure 11: Comparison of axial velocity history of impactor obtained using EE approach and Mesh EE-1 to that obtained using TNWF approach and Mesh TNWF-1 (Case 1).

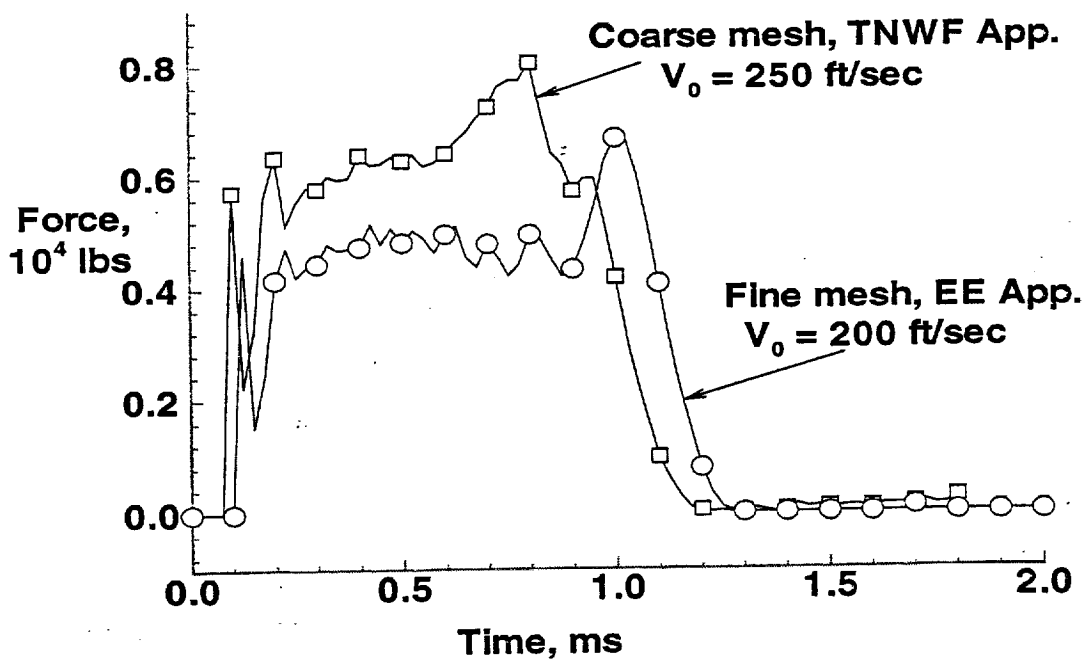


Figure 12: Comparison of axial contact force history of the target obtained using EE approach and Mesh EE-1 to that obtained using TNWF approach and Mesh TNWF-1 (Case 1).

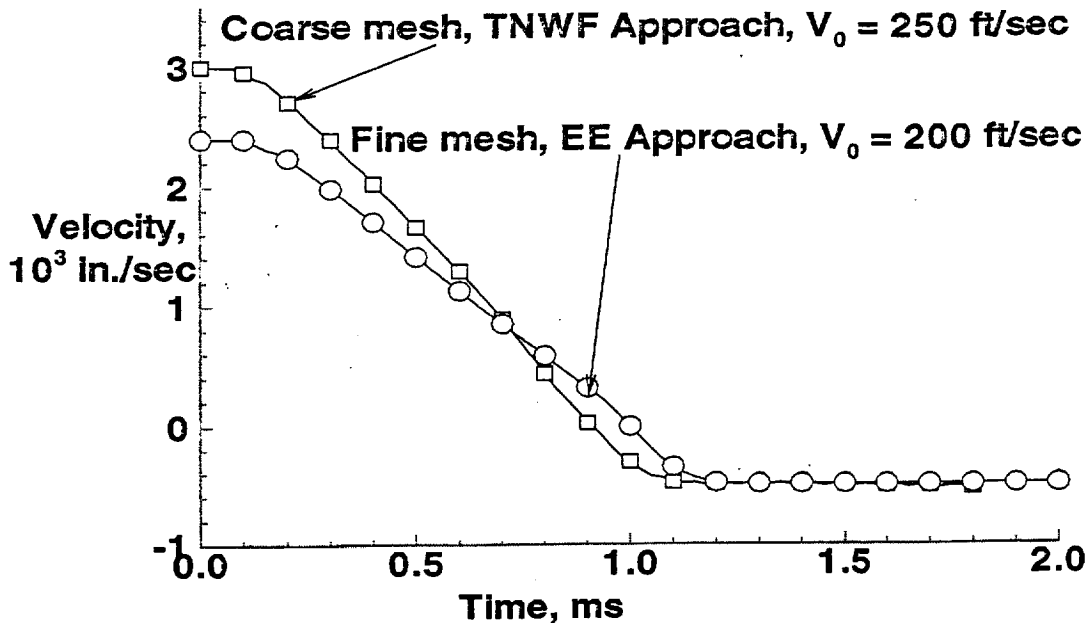


Figure 11: Comparison of axial velocity history of impactor obtained using EE approach and Mesh EE-1 to that obtained using TNWF approach and Mesh TNWF-1 (Case 1).

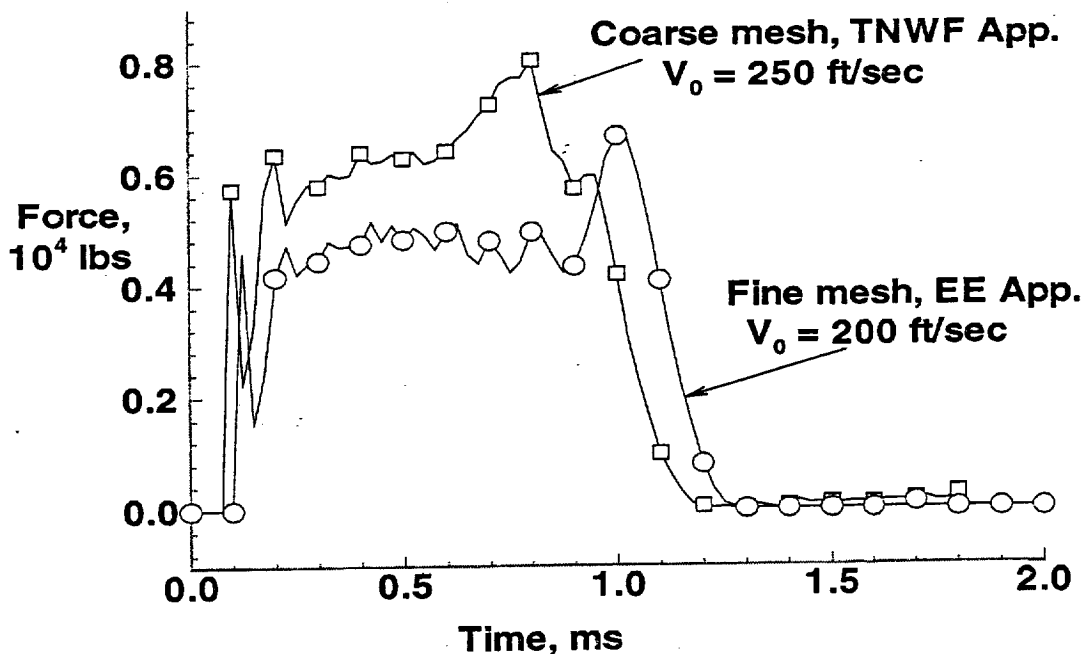


Figure 12: Comparison of axial contact force history of the target obtained using EE approach and Mesh EE-1 to that obtained using TNWF approach and Mesh TNWF-1 (Case 1).

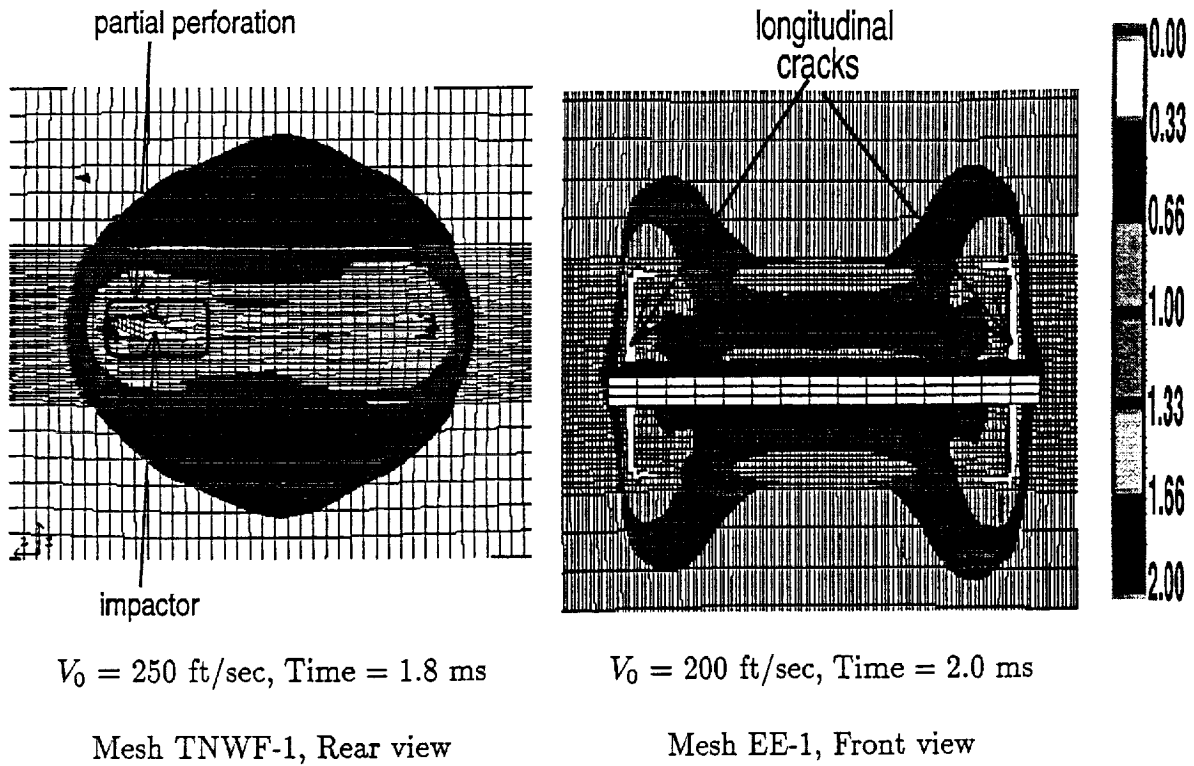


Figure 13: Comparison of effective plastic strain fringe plot of the target between Case 1 (Mesh TNWF-1) and using EE approach with Mesh EE-1 in the vicinity of the impact site.

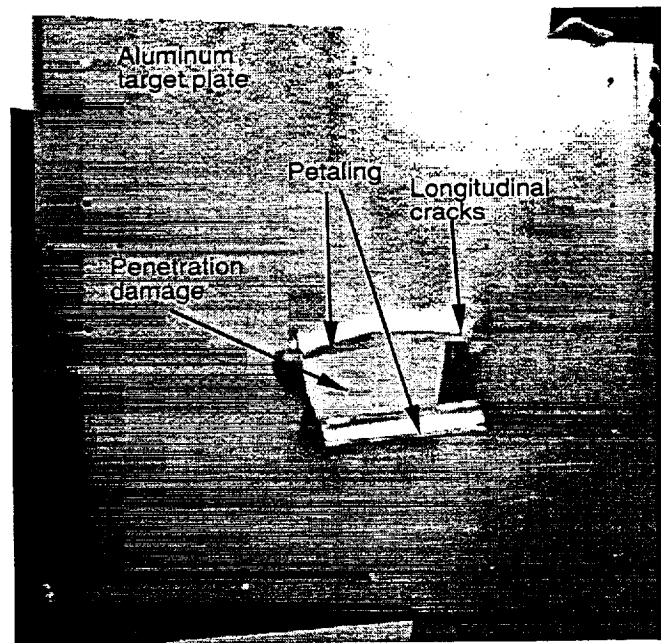
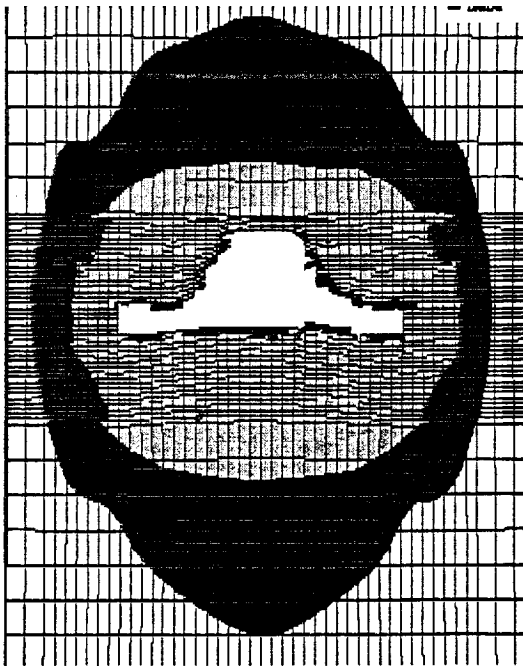
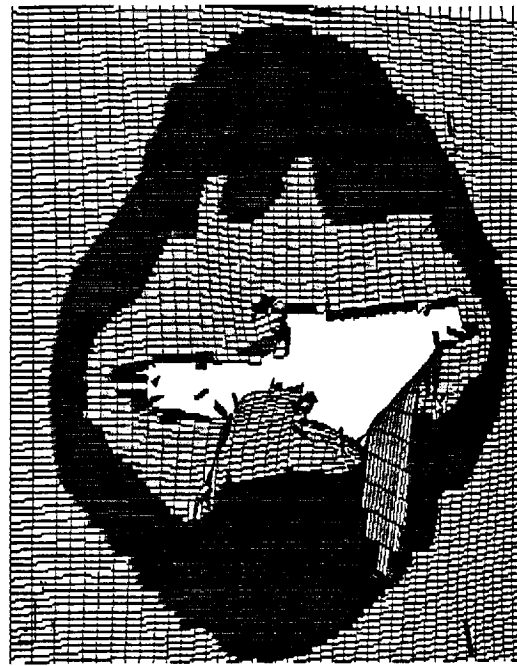


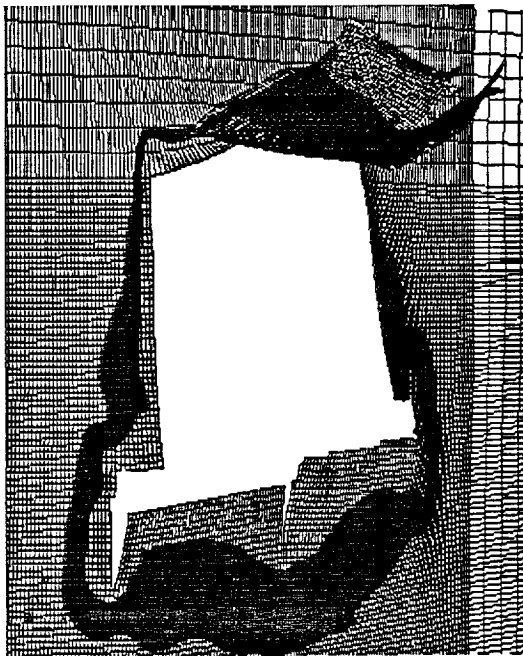
Figure 14: Photograph of damage aluminum target for an impactor initial velocity of 450 ft/sec.



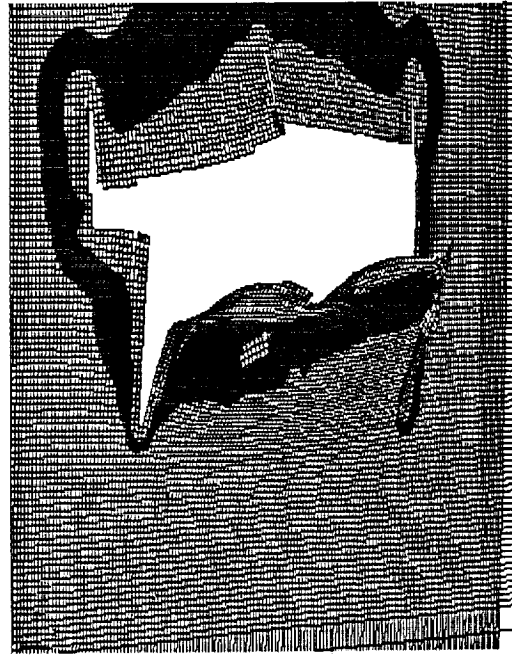
Study 1 (Mesh TNWF-1)



Study 2 (Mesh TNWF-2)



Study 3 (Mesh EE-2)



Study 4 (Mesh EE-2)



Figure 15: Comparison of effective plastic strain fringe plot of the target for Study 1 through 4 in the vicinity of the impact site.

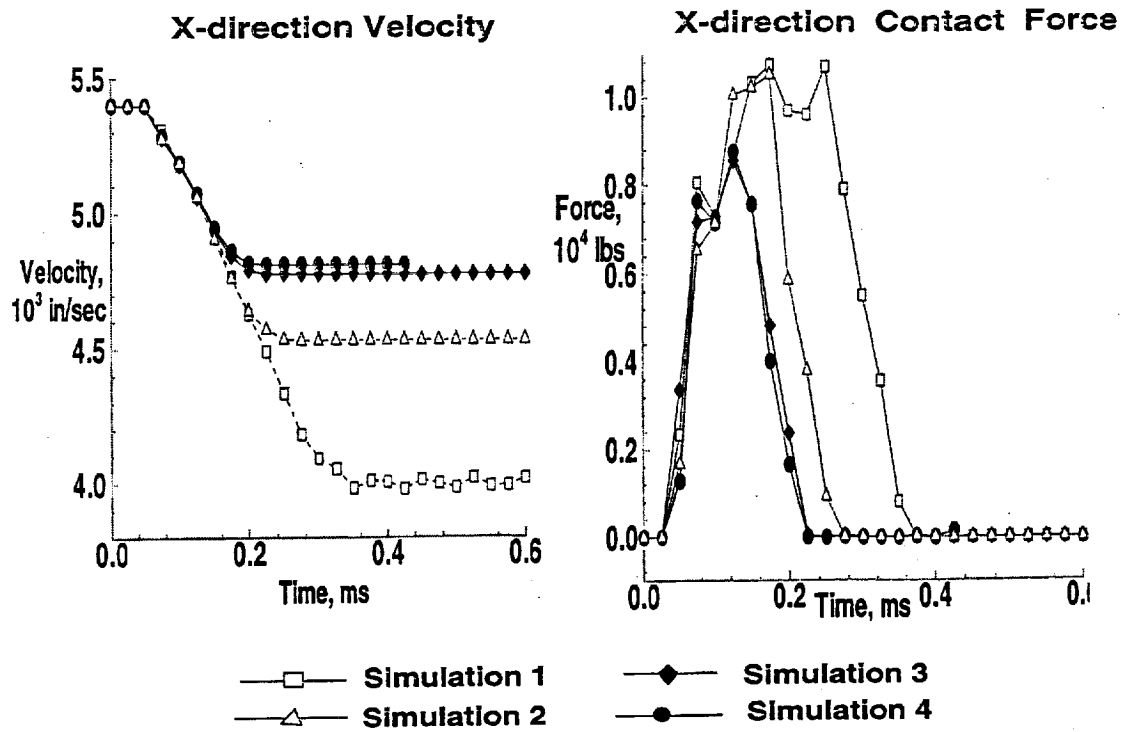


Figure 16: Comparison of axial velocity and axial contact force history of the target for Study 1 through 4.

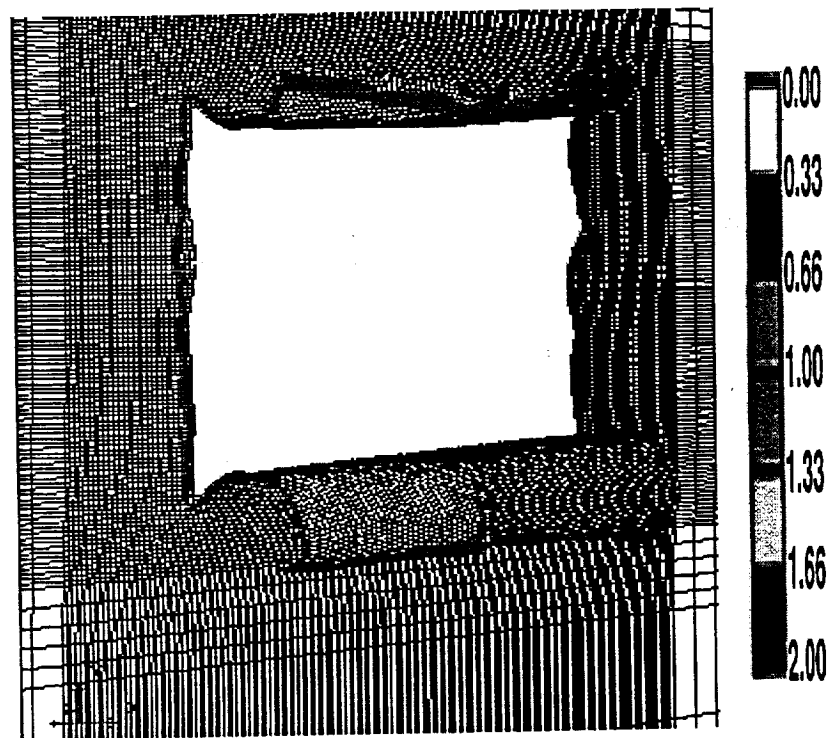


Figure 17: Fringe plot of effective plastic strain of the target for Case 8.

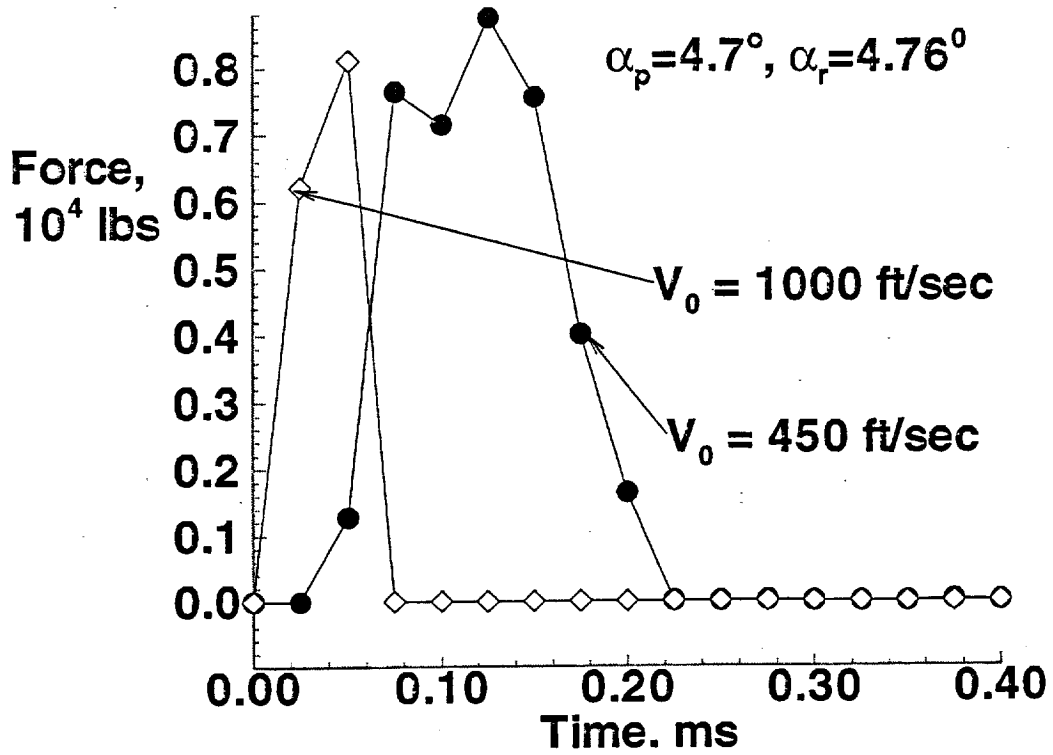


Figure 18: Comparison of axial contact force history of the target for Case 8 and Study 4.

## APPENDIX B

### Optimal Design of Grid-stiffened Panel and Shells with Variable Curvature.

## Abstract

A design strategy for optimal design of composite grid-stiffened panels with variable curvature subjected to global and local buckling constraints is developed using a discrete optimizer. An improved smeared stiffener theory is used for the global buckling analysis. Local buckling of skin segments is assessed using a Rayleigh-Ritz method that accounts for material anisotropy and transverse shear flexibility. The local buckling of stiffener segments is also assessed. Design variables are the axial and transverse stiffener spacing, stiffener height and thickness, skin laminate, and stiffening configuration, where stiffening configuration is herein defined as a design variable that indicates the combination of axial, transverse and diagonal stiffeners in the stiffened panel. The design optimization process is adapted to identify the lightest-weight stiffening configuration and stiffener spacing for grid-stiffened composite panels given the overall panel dimensions, in-plane design loads, material properties, and boundary conditions of the grid-stiffened panel.

## Nomenclature

$a, b$	Axial and transverse stiffener spacing
$h$	Stiffener height
$t$	Skin laminate thickness
$t_s$	Stiffener thickness
$LAMI$	Design variable for stacking sequence of skin laminate
$ICON$	Design variable for stiffening configuration
$\lambda_G$	Global buckling load factor
$\lambda_{sk}$	Buckling load factor for skin segment
$\lambda_1, \lambda_2, \lambda_3$	Buckling load factor for axial, transverse, and diagonal stiffener segments

## Introduction

The use of composite materials for aircraft primary structures can result in significant benefits on aircraft performance and structural cost. Such applications of composites materials are expected to result in a 30-40 percent weight savings and a 10-30 percent cost reduction compared to conventional metallic structures. Structural configurations with variable curvature are widely used for aircraft fuselage and wing components. The variable curvature configuration for these structures is due to aerodynamic and functional considerations. Hence optimum design of stiffened composite panel or shell structures with variable curvature is important for aerospace structural design.

A summary of the research work conducted on the design optimization of stiffened panels and shells is given in Reference [1]. This summary of research work on stiffened panels shows that researchers have examined stiffened flat panels, cylindrical panels and circular cylinders. Most of these references address axially or orthogonally stiffened panels or cylinders, with the exception of references [2], [3], [4] and [5] which deal with grid-stiffened panels or shell. A gradient-based optimizer has been mostly

used, and a genetic algorithm has been used where researchers have treated the design variables as discrete variables (e.g., Ref. [6] and [7]).

Reference [1] presents an analysis and design strategy for grid-stiffened composite panels subjected to combined loads and a global buckling design constraint. Local buckling analyses for skin and stiffener segments are included so that the stiffened panel can be assessed for such local buckling. The global buckling constraint for the grid-stiffened panel is important to prevent localized skin buckling. This constraint reduces the loss of aerodynamic performance caused by the buckling of wing or fuselage surfaces and prevents the failure of a panel by stiffener-skin separation ([8]) after buckling. Design variables are the axial and transverse stiffener spacings, the stiffening configuration, the skin laminate stacking sequence, and the height and thickness of the stiffener. A genetic algorithm is used as the optimization tool for evolving the design since the stiffener spacings, stiffening configuration, stiffener thickness, and skin laminate are discrete design variables. The literature survey in Ref. [1] also indicates no references to work on optimization of panel or shell with variable curvature.

A buckling analysis method for anisotropic shells with variable curvature is presented in Ref. [9]. A review of the past research work on vibration and buckling of variable curvature shell is also presented in Ref. [9]. A segmented approach where displacement fields within each segment are represented by Bezier polynomials and a first-order shear-deformation theory is used in Ref. [9]. Continuity of displacements at the junctures of adjacent segments are imposed using  $C^0$  and  $C^1$  conditions obtained from the properties of the Bezier control points. The shell with variable curvature is assumed to consist of two or more curved panels of constant curvature which is representative of fuselage or wing structures. Bezier polynomials are used in the axial and circumferential directions to represent the displacement fields. Reference [9] provides an analysis method which is in good agreement with results from finite element solutions. The method involved significantly less computational effort and less time for model preparation than needed for finite element solutions.

## Buckling Analysis

The coordinate system and the displacement directions for a noncircular shell are shown in Figure 1. Any point in the wall of the shell is specified by means of a curvilinear coordinate system  $x$ ,  $y$  and  $z$ , where  $x$  is the axial coordinate fixed to mid-surface,  $y$  is the circumferential coordinate which follows the median line of the transverse cross section, and  $z$  is the radial coordinate normal to both  $x$  and  $y$ . The noncircular shell is assumed to consist of two or more segments in the circumferential direction, each of constant radius. The normal and tangent vectors of the two segments at a juncture are equal as shown in Figure 1, where  $\vec{n}_1 = \vec{n}_2$  and  $\vec{t}_1 = \vec{t}_2$ .

Fourier series and Bezier polynomials are used in the axial and circumferential directions, respectively, to represent the displacement fields. The Bezier polynomial is given by

$$f_i(n, \nu) = \frac{n!}{(i-1)! (n-i+1)!} \nu^{i-1} (\nu-1)^{n-i+1} \quad (1)$$

where  $n$  denotes the order of the polynomial and  $0 \leq \nu \leq 1$ . For a Bezier polynomial of order  $n$ , there are  $(n + 1)$  control points. Any point on the surface of the segment is given by a parametric function of the form

$$P_{rs}(\xi, \eta) = \sum_{r=1}^X \sum_{s=1}^Y T_r(\xi) f_s(\eta) q_{rs} \quad (2)$$

where  $T_r$  is a Fourier term,  $f_s$  is a quintic Bezier polynomial,  $X$  is the number of Fourier terms in the axial direction,  $Y$  is the number of control points in the circumferential direction, respectively, and  $q_{rs}$  are the Bezier control points. The displacement vector can be written as

$$\begin{bmatrix} U_0 & V_0 & W & \phi_x & \phi_y \end{bmatrix}_i^T = \begin{bmatrix} C(\bar{\xi})_r f(\eta)_s & 0 & 0 & 0 & 0 \\ 0 & S(\bar{\xi})_r f(\eta)_s & 0 & 0 & 0 \\ 0 & 0 & S(\bar{\xi})_r f(\eta)_s & 0 & 0 \\ 0 & 0 & 0 & C(\bar{\xi})_r f(\eta)_s & 0 \\ 0 & 0 & 0 & 0 & S(\bar{\xi})_r f(\eta)_s \end{bmatrix}_i \begin{Bmatrix} q_{1rs} \\ q_{2rs} \\ q_{3rs} \\ q_{4rs} \\ q_{5rs} \end{Bmatrix}_i \quad (3)$$

where  $U_0$  and  $V_0$  are the axial and transverse membrane displacements, respectively,  $W$  is the normal displacement.  $\phi_x$  and  $\phi_y$  are the curvatures,  $C(\bar{\xi})_r = \cos(m\pi\xi)_r$ , and  $S(\bar{\xi})_r = \sin(m\pi\xi)_r$ . Coordinates  $\xi$  and  $\eta$  are defined as

$$\begin{aligned} \xi &= x / L \\ \eta &= (y - y_i) / (y_{i+1} - y_i) \end{aligned} \quad (4)$$

with  $0 \leq \xi, \eta \leq 1$ . Subscript  $j = 1, 2, 3, \dots (XY)$ . The control points for each degree of freedom can be used to impose boundary conditions on each degree of freedom in the circumferential direction and the boundary condition along  $\xi = 0$  and 1 are simply support conditions resulting from the choice of Fourier series used.

Continuity of displacement functions along segment junctures are obtained by using the relations between control points of the adjacent segments based on  $C^0$  continuity since the buckling analysis involves first-order shear deformation. The segments are joined in a way similar to the conventional finite elements so as to provide modeling for panel or shell of variable curvature. The above displacement vector is used with in an energy formulation to determine the buckling load. Sanders-Koiter shell theory ([10]) is also used in the formulation. The above formulation is computationally more efficient than the formulation presented in Ref. [9] where Bezier polynomials are used in the axial and circumferential directions. Hence the formulation using Fourier series and Bezier polynomials is more suitable for use with an optimizer such as the genetic algorithm.

An improved smeared stiffener theory ([11]) is used with the above buckling analysis to obtain the global buckling load of the variable curvature panel or shell. The local buckling of the skin is assessed using the formulation presented in Reference [12] for triangular skin segment and Reference [13] for quadrilateral skin segment. The

cripling of the stiffener segment is assessed using the method presented in Reference [2].

## Problem Definition

The present design problem is to minimize the weight per unit area of a grid-stiffened composite panel or shell with variable curvature given the design loading condition, the length and width of the panel, the material properties for the skin and stiffeners, and the boundary conditions for the panel or shell. As shown in Figure 2, a general grid-stiffened panel may be considered as an assembly of a repetitive unit or a unit cell. A unit cell contains both skin and stiffener elements. The design variables include stiffener spacings ( $a$ ,  $b$ ), skin stacking sequence or laminate ( $LAMI$ ), stiffening configuration ( $ICON$ ), stiffener thickness ( $t_s$ ), and stiffener height ( $h$ ). The stiffener spacings ( $a$ ,  $b$ ), stiffener height ( $h$ ), and stiffener thickness ( $t_s$ ) are shown in Figure 2 for the unit cell. Also shown in Figure 2 is the skin thickness ( $t$ ) which depends on the the number of plies in the skin. The stiffening configuration depends on the combination of axial, transverse and diagonal stiffeners in the unit cell (Figure 2). For manufacturing and assembly reasons, all stiffeners are assumed to be of the same height and thickness. The design sought here is a panel of minimum weight in a certain design space which buckles globally at the design loads. This design problem can be defined by setting up the optimization procedures in the following way. First, the global buckling load is assumed to be a scalar multiple of the design loads and has the form

$$(N_x)_{cr} = \lambda_G N_x, \quad (N_y)_{cr} = \lambda_G N_y, \quad (N_{xy})_{cr} = \lambda_G N_{xy} \quad (5)$$

where  $N_x$ ,  $N_y$ ,  $N_{xy}$  are the applied in-plane prebuckling loads. These values represent the design loads for the grid-stiffened panel. Second, the design constraints imposed on the panel include the following requirements.

1. The critical buckling load should be greater than or equal to the design loads, that is,  $\lambda_G \geq 1$ .
2. The skin segments should not buckle at the critical buckling load, that is,  $\lambda_{sk} \geq 1$ .
3. The stiffener segments should not cripple at the critical buckling load, that is,  $\lambda_1, \lambda_2, \lambda_3 \geq 1$  where  $\lambda_1, \lambda_2, \lambda_3$  are the crippling load factors of the x-direction (axial) stiffener, y-direction (transverse) stiffener and diagonal stiffener, respectively.

The local buckling load factors of each stiffener segment type and skin segment is

$$\lambda_i = \frac{\text{critical load of local segment}}{\text{load in local segment due to } \lambda_G \times (N_x, N_y, N_{xy})} \quad (6)$$

where  $i = 1, 2, 3$  and  $sk$  and the general form of each constraint equation is written as

$$g_j = \left( \frac{1}{\lambda_j} - 1 \right) \leq 0.0 \quad j = 1, \dots, N_c \quad (7)$$

Finally, since the minimum weight panel design is sought, the “fitness” measure is related to the reciprocal of the panel weight with the buckling constraints included. Hence the “fitness” expression based on an exterior penalty function approach is

$$\text{Fitness} = \left( \frac{Q}{F(\mathbf{X}, r_i)} \right) = \text{Max} \frac{Q}{W(\mathbf{X}) + r_i \sum_j^{N_c} (|g_j(\mathbf{X})| + g_j(\mathbf{X}))^2} \quad (8)$$

where

$\mathbf{X}$  = design variable vector

$F(\mathbf{X}, r_i)$  = modified objective function

$W(\mathbf{X})$  = weight of panel per unit area

$r_i \sum_j^{N_c} (|g_j(\mathbf{X})| + g_j(\mathbf{X}))^2$  = penalty function

$Q$  = normalizing constant

$N_c$  = number of design constraints

$r_i$  = penalty parameter

$i$  = generation or iteration cycle in the optimization procedure

### Design Process Based on a Genetic Algorithm

The design process begins with a random selection of the specified number of designs which comprise the initial population (i.e., first generation) for the genetic algorithm. The problem parameters such as material properties, panel length and width, boundary conditions of the panel, and design loads are input into the analysis processor routine. The buckling analyses are performed which provide the critical eigenvalues for the global buckling response of the grid-stiffened panel, and the local buckling response of the skin and stiffener segments. The weight per unit area of the grid-stiffened panel is also computed. This procedure is repeated for each design configuration in the population. The “fitness” processor then evaluates the “fitness” of each design using Equation (8) and assigns a rank based on the fitness expression or the objective function. The current population of design configurations is then assessed by the genetic operators (crossover, mutation, and permutation) to create a new population of design configurations for the subsequent generations which combines the most desirable characteristics of the previous generations. Designs from previous generations may be replaced by new ones (i.e., children) except for the “most fit” designs (i.e., parents) which are always included in the next generation. The process is repeated until design convergence is obtained. Convergence is defined herein by specifying a maximum number of generations ( $NSTOP$ ) that may occur without any improvement in the “most fit” design. The design procedure is demonstrated on flat and curved grid-stiffened panels in Ref. [1].

### Numerical Results

A non-circular grid-stiffened composite panel representative of a generic rotorcraft fuselage structural component is designed to demonstrate the capabilities of the present design optimization tool. The non-circular panel is shown in Figure 3. Only half of the panel is considered in the computational modeling due to symmetry.

The half panel consists of five curved segments as shown in Figure 3. The panel is considered to be simply supported and symmetry condition are used in the modeling.

The panel is optimized for a load case with 2000.0 lbs/in. of shear, which is considered to be the critical load case for this panel. The termination criterion (*NSTOP*) is 20 generations; and the population size is set to eight. The probabilities used for crossover, mutation, and permutation are 1.0, 0.10, and 0.95, respectively. Also, the penalty parameter  $r_i$  is kept constant for all iterations since the genetic algorithms maximize Equation (8) more efficiently. The design variables are the stiffener height and thickness and the skin laminate. The stiffeners are made of 0° material only. The stiffening configuration considered is axial and diagonal stiffeners, i.e., *ICON*=5. Two stiffener spacings are considered;

- Case 1:  $a = 4.000$ -in. and  $b = 6.880$ -in.
- Case 2:  $a = 3.428$ -in. and  $b = 5.931$ -in.

These two stiffener spacings result in a stiffening configuration which is very close to isogrid configuration. The local analysis of the skin segment and stiffener segment are performed for segment No. 1 where the radius of curvature is the largest and local buckling of the skin segment is likely to occur in this segment first.

The buckling analysis were performed using one segment for each curved segment and 10 Fourier terms in in the axial direction (i.e.,  $X=10$ ). The nominal ply mechanical properties used are:  $E_{11} = 20.2$  Msi;  $E_{22} = 1.9$  Msi;  $G_{12} = G_{13} = G_{23} = 0.73$  Msi and  $\nu_{12} = 0.3$ . The mass density of the material  $\rho$ , is 0.0570 lbs/in.<sup>3</sup>

Case 1:  $a = 4.000$ -in. and  $b = 6.880$ -in.

In the first case, the panel has an axial stiffener spacing ( $a$ ) of 4.00-in. and a transverse stiffener spacing ( $b$ ) of 6.880-in. The design space for the skin laminate and stiffener height and thickness is shown in Table 1. Each design variable can assume eight discrete values. For example when  $LAMI = 1$ , then the skin stacking sequence is  $[\pm 45/0]_{2s}$ . The aspect ratio of the stiffener ( $h/t_s$ ) is kept between 3 and 9 for manufacturing reasons.

The results for the optimization are shown in Table 2 where the five best designs are shown. All the designs shown in Table 2 buckle globally at their respective global buckling load since the skin segment buckling load factor and the diagonal stiffener buckling load factor are greater than one. The best design is the first design since it is the lightest. The third and fourth design have a global buckling load factor slightly less than one and are still considered good design. The fifth design has no constraints violation, however the weight of the panel is heavier than the other four panels.

Case 2:  $a = 3.428$ -in. and  $b = 5.931$ -in.

In the second case, the panel has an axial stiffener spacing ( $a$ ) of 3.428-in. and a transverse stiffener spacing ( $b$ ) of 5.931-in. The design space for the skin laminate and stiffener height and thickness is same as that of Case 1 which is shown in Table 1.

The results for the optimization are shown in Table 3 where the three best designs are shown. All the designs shown in Table 2 buckle globally at their respective global buckling load since the skin segment buckling load factor and the diagonal stiffener buckling load factor are greater than one. The best design is the first design since it is the lightest. The second design has a performance close to that of the first design and its weight per unit area is close to that of the first one. The third design is heavier than the first and second design.

### Concluding Remarks

A minimum-weight design optimization tool with buckling constraints has been developed for grid-stiffened panels with variable curvature using global and local buckling analyses and a genetic algorithm. The variable curvature of the shell is modeled as an assembly of panels with constant curvature. Design variables used are axial and transverse stiffener spacing, stiffener height and thickness, skin-laminate stacking sequence, and stiffening configuration. A pool of acceptable designs is obtained by the genetic algorithm.

### References

- [1] Jaunky, N., Knight, N. F. and Ambur, D., "Optimal Design of Grid-stiffened Composite Panels Using Global and Local Buckling Analyses," *Journal of Aircraft*, Vol. 35, No. 3, 1998, pp. 478-486.
- [2] Reddy, A. D., Valisetty, Rao R., and Rehfield, L. W., "Continuous Filament Wound Composite Concepts for Aircraft Fuselage Structures," *Journal of Aircraft*, Vol. 22, No. 3, March 1985, pp. 249-255.
- [3] Phillips, J. L. and Gurdal, Z., "Structural Analysis and Optimum Design of Geodesically Stiffened Composite Panels," Report CCMS-90-05, Center for Composite Materials and Structures, Virginia Polytechnic Institute and State University, Blacksburg, VA, July 1990.
- [4] Gendron, G., and Gurdal, Z., "Optimal Design of Geodesically Stiffened Composite Cylindrical Shell," Proceedings of 33rd AIAA/ASME/ASCE/AHS/ASC Structures, Structural Dynamics, and Materials Conference, Dallas, TX, AIAA Paper No. 92-2306-CP, April 13-15, 1992, pp. 2431-2441.
- [5] Bushnell, D., "Recent Enhancements to PANDA2," Proceedings of the 37<sup>th</sup> AIAA/ASME /ASCE/AHS/ASC Structures, Structural Dynamics, and Materials Conference, Salt Lake City, UT, AIAA Paper No. 96-1337-CP, April, 15-17, 1996, pp. 126-182.
- [6] Nagendra, S., Haftka, R. T., and Gurdal, Z., "Design of a Blade Stiffened Composite Panel by Genetic Algorithm," Proceedings of 34th

AIAA/ASME/ASCE/AHS/ASC Structures, Structural Dynamics and Materials Conference, AIAA Paper No. 93-1584-CP, April 1993, La Jolla, CA, pp. 2418-2436.

- [7] Harrison, P. N., Leriche, R., and Haftka, R. T., "Design of Stiffened Panels by Genetic Algorithm and Response Surface Approximations," Proceedings of 36<sup>th</sup> AIAA/ASME/ASCE/ AHS/ASC Structures, Structural Dynamics, and Materials Conference, New Orleans, LA, AIAA Paper No. 95-1163-CP, April 10-13, 1995, pp. 58-68.
- [8] Rouse, M., and Ambur, D. R., "Damage Tolerance and Failure Analysis of a Geodesically Stiffened Structure Loaded in Axial Compression," AIAA Paper No. 94-1534, Proceedings of the 35th AIAA/ASME/ASCE/AHS/ASC Structures, Structural Dynamics, and Materials Conference, Hilton Head, SC, April 18-21, 1994, pp. 1691-1698.
- [9] Jaunky, N., Knight, N. F. and Ambur, D., "Buckling Analysis of Anisotropic Curved Panels and Shells with Variable Curvature," *Composite Structures*, Vol. 43, 1999, pp. 321-329.
- [10] Sanders, J. L. Jr., "An Improved First Approximation Theory for Thin Shells," NASA Report R-24, 1959.
- [11] Jaunky, N., Knight, N. F., and Ambur, D. R., "An Improved Smeared Theory for Buckling Analysis of Grid-Stiffened Composite Panels," *Composite: Part B* (formerly *International Journal for Composite Engineering* ), Vol. 27B, No. 5, 1996, pp. 519-526.
- [12] Jaunky, N., Knight, N. F., and Ambur, D. R., "Buckling of Arbitrary Quadrilateral Anisotropic Plates," *AIAA Journal*, Vol. 33, May 1995, pp. 938-944.
- [13] Jaunky, N., Knight, N. F., and Ambur, D. R., "Buckling Analysis of General Triangular Anisotropic Plates using Polynomials," *AIAA Journal*, Vol. 33, December 1995, pp. 2414-2417.

Table 1 Design space for skin laminate and stiffener height and thickness.

Integer value	LAMI ply thickness = 0.004-in.	$h$ (in.)	$t$ (in.)
1	$[\pm 45/0]_{2s}$	0.25	0.032
2	$[\pm 45/90]_{2s}$	0.26	0.042
3	$[\pm 45/0/90]_{2s}$	0.27	0.048
4	$[\pm 45/0_2]_{2s}$	0.28	0.054
5	$[\pm 45/90_2]_{2s}$	0.29	0.060
6	$[\pm 45/0_2/90]_{2s}$	0.30	0.066
7	$[\pm 45/0/90_2]_{2s}$	0.31	0.072
8	$[\pm 45/0_2/90_2]_{2s}$	0.32	0.078

Table 2 Best designs obtained by the genetic algorithm for stiffener spacing of  $a = 4.000$ -in. and  $b = 6.880$ -in. (Case 1).

Design variables	Weight, (lbs/ft <sup>2</sup> )	Buckling load factors
$h = 0.28$ in., $t_s = 0.066$ in., $LAMI = [\pm 45/0]_{2s}$	0.788	$\lambda_G = 1.039$ , $\lambda_{sk} = 2.493$ $\lambda_3 = 1.150$
$h = 0.29$ in., $t_s = 0.066$ in., $LAMI = [\pm 45/0]_{2s}$	0.793	$\lambda_G = 1.099$ , $\lambda_{sk} = 2.367$ $\lambda_3 = 1.045$
$h = 0.28$ in., $t_s = 0.066$ in., $LAMI = [\pm 45/90]_{2s}$	0.788	$\lambda_G = 0.985$ , $\lambda_{sk} = 2.559$ $\lambda_3 = 1.210$
$h = 0.26$ in., $t_s = 0.072$ in., $LAMI = [\pm 45/0]_{2s}$	0.790	$\lambda_G = 0.982$ , $\lambda_{sk} = 2.645$ $\lambda_3 = 1.574$
$h = 0.28$ in., $t_s = 0.078$ in., $LAMI = [\pm 45/0/90]_{2s}$	0.943	$\lambda_G = 1.243$ , $\lambda_{sk} = 3.430$ $\lambda_3 = 1.369$

Table 3 Best designs obtained by the genetic algorithm for stiffener spacing of  $a = 3.428$ -in. and  $b = 5.931$ -in. (Case 2).

Design variables	Weight, (lbs/ft <sup>2</sup> )	Buckling load factors
$h = 0.26$ in., $t_s = 0.066$ in., $LAMI = [\pm 45/0]_{2s}$	0.799	$\lambda_G = 1.026$ , $\lambda_{sk} = 3.355$ $\lambda_3 = 1.413$
$h = 0.27$ in., $t_s = 0.066$ in., $LAMI = [\pm 45/90]_{2s}$	0.804	$\lambda_G = 1.025$ , $\lambda_{sk} = 3.278$ $\lambda_3 = 1.358$
$h = 0.28$ in., $t_s = 0.078$ in., $LAMI = [\pm 45/0/90]_{2s}$	0.969	$\lambda_G = 1.367$ , $\lambda_{sk} = 4.153$ $\lambda_3 = 1.397$

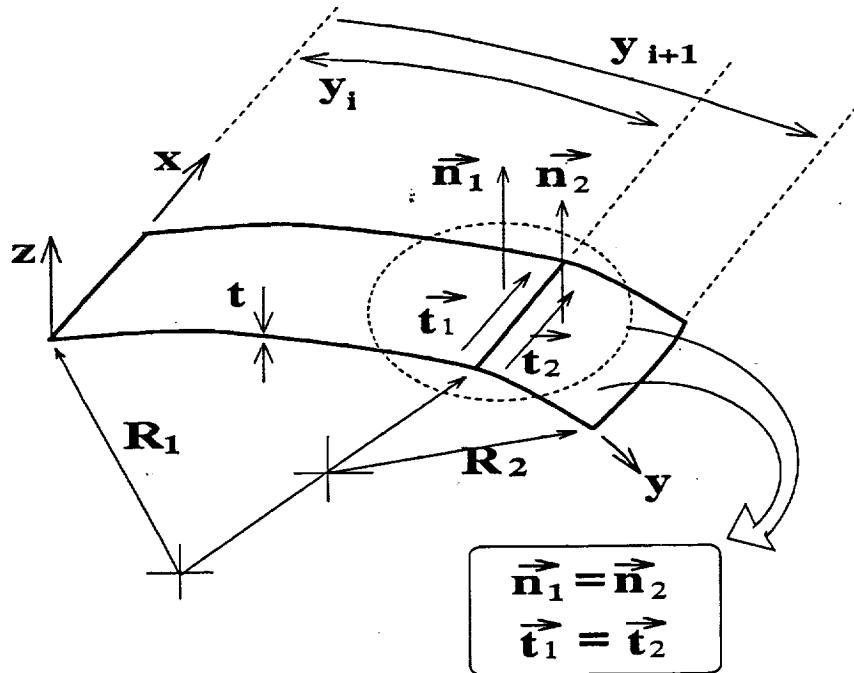


Figure 1: Coordinate system and geometry of shell with variable curvature.

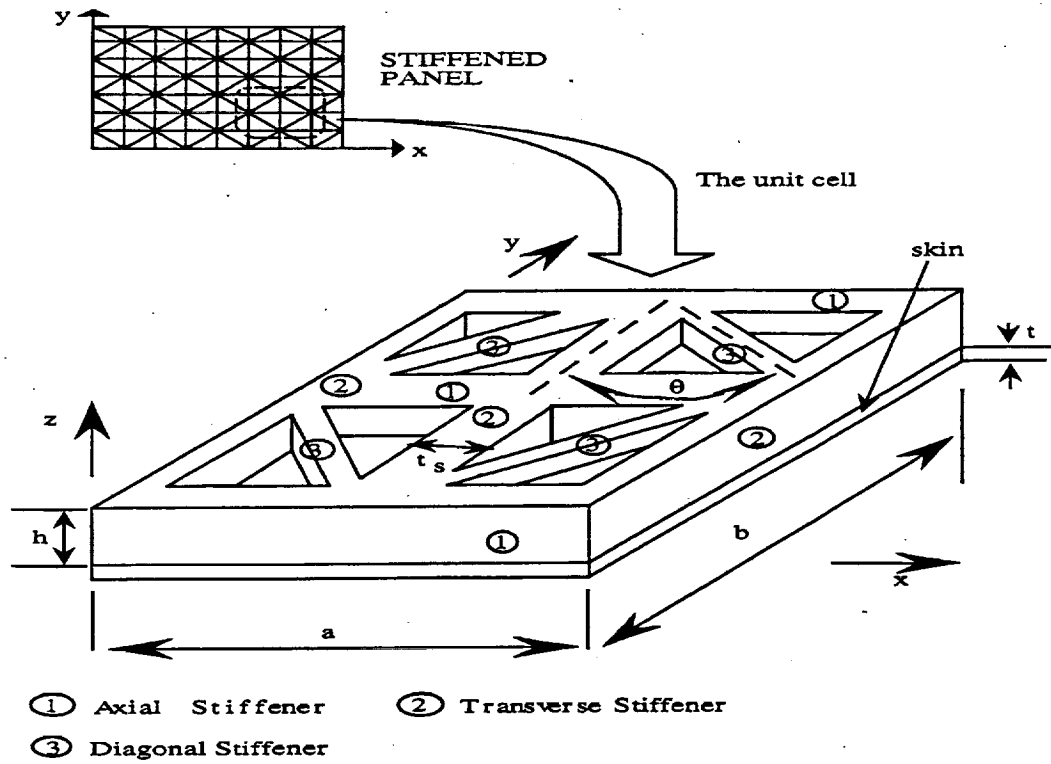


Figure 2: Unit cell of the grid-stiffened panel and design variables.

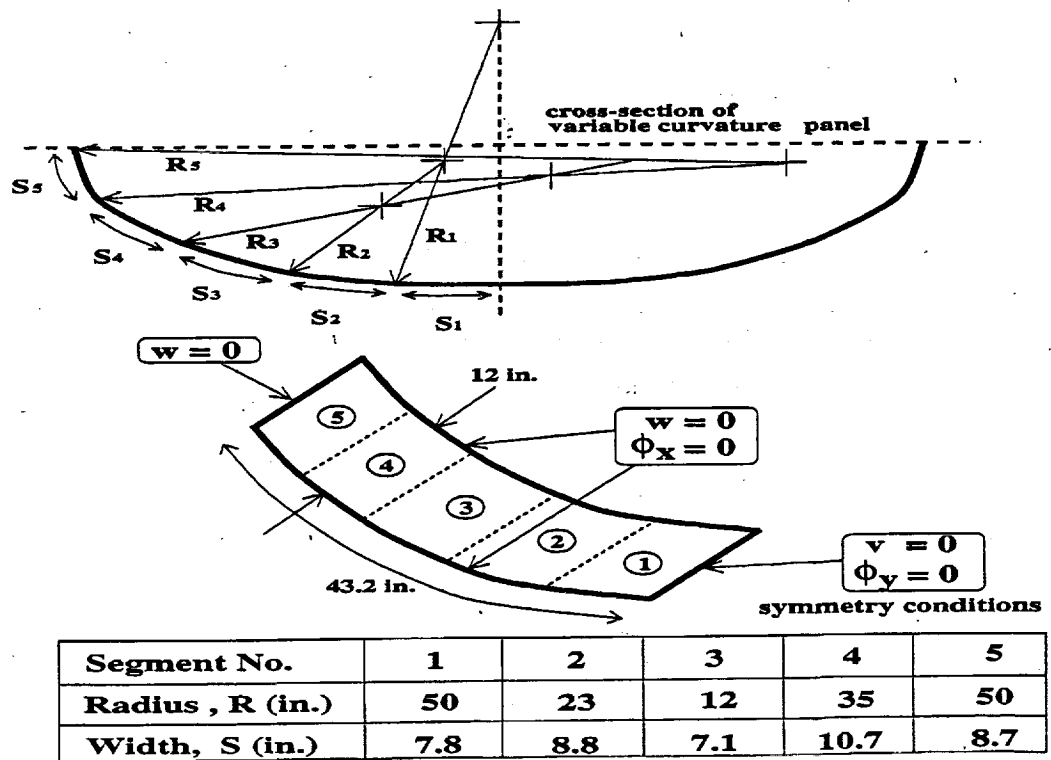


Figure 3: Cross-section and boundary conditions of variable curvature panel.